Spectral retrieval of latent heating profiles from TRMM PR data. Part III: Moistening Estimates over Tropical Ocean Regions

Shoichi Shige, Yukari N. Takayabu, and Wei-Kuo Tao

Submitted to Appl. Meteor. Clim.

Popular Summary

The global hydrological cycle is central to the Earth's climate system, with rainfall and the physics of precipitation formation acting as the key links in the cycle. Two-thirds of global rainfall occurs in the tropics with the associated latent heating (LH) accounting for three-fourths of the total heat energy available to the Earth's atmosphere. In the last decade, it has been established that standard products of LH from satellite measurements, particularly TRMM measurements, would be a valuable resource for scientific research and applications. Such products would enable new insights and investigations concerning the complexities of convection system life cycles, the diabatic heating controls and feedbacks related to meso-synoptic circulations and their forecasting, the relationship of tropical patterns of LH to the global circulation and climate, and strategies for improving cloud parameterizations in environmental prediction models.

However, the LH and water vapor profile or budget (called the apparent moisture sink, or Q2) is closely related. This paper presented the development of an algorithm for retrieving Q2 using TRMM precipitation radar. Since there is no direct measurement of LH and Q2, the validation of algorithm usually applies a method called consistency check. Consistency checking involving Cloud Resolving Model (CRM)-generated LH and Q2 profiles and algorithm-reconstructed is a useful step in evaluating the performance of a given algorithm. In this process, the CRM simulation of a time-dependent precipitation process (multiple-day time series) is used to obtain the required input parameters for a given algorithm. The algorithm is then used to "*reconstruct*" the heating and moisture profiles that the CRM simulation originally produced, and finally both sets of conformal estimates (model and algorithm) are compared each other.

The results indicate that discrepancies between the reconstructed and CRM-simulated profiles for Q2, especially at low levels, are larger than those for latent heat. Larger discrepancies in Q2 at low levels are due to moistening for non-precipitating region that algorithm cannot reconstruct. Nevertheless, the algorithm-reconstructed total Q2 profiles are in good agreement with the CRM-simulated ones.

Spectral retrieval of latent heating profiles from TRMM PR data.

Part III: Moistening Estimates over Tropical Ocean Regions

Shoichi Shige[1,*], Yukari N. Takayabu[2,3], and Wei-Kuo Tao[4]

[1] *Department of Aerospace Engineering, Osaka Prefecture University, Osaka, Japan*

[2] *Center for Climate System Research, University of Tokyo, Chiba, Japan*

[3] *Institute of Observational Research for Global Change, Japan Agency for Marine-Earth Science and Technology, Kanagawa, Japan*

[4] *Laboratory for Atmospheres, NASA Goddard Space Flight Center, Greenbelt, Maryland*

J. Appl. Meteor. Clim.

March 2007

* **Corresponding author address:** Dr. Shoichi Shige, Department of Aerospace Engineering, Osaka Prefecture University, 1-1 Gakuen-cho, Sakai, Osaka 599-8531, Japan
E-mail: shige@aero.osakafu-u.ac.jp, Tel/Fax: +81-72-254-9245

Abstract

The Spectral Latent Heating (SLH) algorithm was developed for the Tropical Rainfall Measuring Mission (TRMM) precipitation radar (PR) in part I of this study and improved in part II to estimate apparent heat source (Q_1) profiles. In this paper, the SLH algorithm is used to estimate apparent moisture sink (Q_2) profiles. Procedure of Q_2 retrieval is the same as that of heating retrieval (Part I, II) except for using the Q_2 profile lookup tables derived from numerical simulations of tropical cloud systems from the Tropical Ocean Global Atmosphere (TOGA) Coupled Ocean–Atmosphere Response Experiment (COARE) utilizing a cloud-resolving model (CRM).

The Q_2 profiles were reconstructed from CRM-simulated parameters [precipitation top height (PTH), precipitation rates at the surface and melting level, and rain type] with the COARE table and compared then to CRM-simulated "true" Q_2 profiles, which were computed directly from the model water vapor equation. COARE, GATE, SCSMEX, and KWAJEX periods were used for the consistency check. The consistency check indicates that discrepancies between the SLH-reconstructed and CRM-simulated profiles for Q_2, especially at low levels, are larger than those for Q_1. Larger discrepancies in Q_2 at low levels are due to moistening for non-precipitating region that SLH cannot reconstruct. Nevertheless, the SLH-reconstructed total Q_2 profiles are in good agreement with the CRM-simulated ones.

The SLH algorithm was applied to PR data, and the results compared to Q_2 profiles derived diagnostically from SCSMEX sounding data. Although discrepancies between the SLH-retrieved and sounding-based profiles for Q_2 are larger than those for heating, key features of the vertical profiles agree well. The Q_2 drying magnitudes are smaller than the sounding-derived magnitudes in the upper troposphere. This is because the SLH algorithm is severely limited by the inherent sensitivity of the PR that can detect only precipitation-sized particles.

The SLH algorithm was also applied to PR data for February 1998 (El Niño) and February 1999 (La Niña). The differences in the SLH-estimated Q_2 between February 1998 and February 1999 are consistent with those in the SLH-estimated heating between February 1998 and February 1999. It is also shown that the SLH algorithm can estimate differences of Q_2 between the western Pacific and the Atlantic Ocean as well as those of heating, which are consistent with the results from the budget study.

1. Introduction

The Tropical Rainfall Measuring Mission (TRMM; Simpson et al. 1988, 1996; Kummerow et al. 2000), a joint Japanese-U.S. cooperative Earth Probe satellite, was successfully launched in 1997 to advance understanding of the global energy and water cycle. The TRMM satellite has been in operation for more than 9 years, providing the distribution of rainfall throughout the Tropics using microwave observations from the Precipitation Radar (PR) and the TRMM Microwave Imager (TMI). Estimating vertical profiles of latent heating released by precipitating cloud systems is one of the key objectives of TRMM, together with accurately measuring the horizontal distribution of tropical rainfall (see a review by Tao et al. 2006).

The PR is the first space-borne precipitation radar and can provide height information based upon the time delay of the precipitation-backscattered return power (Kozu et al. 2001; Okamoto 2003). This allows for vertical profiles of precipitation to be obtained directly over the global Tropics (Iguchi et al. 2000). The classification between convective and stratiform regions of mesoscale convective systems (MCS) became more straightforward utilizing observed precipitation profiles (Awaka et al. 1998). The accuracy of this classification is very important for estimating latent heating because differences in diabatic heating profiles exist between convective and stratiform regions of MCSs (Houze 1982; Johnson and Young 1983). For convective regions of MCSs, the heating profile has warming at all levels with a maximum at midlevels, whereas in stratiform regions there is a warming peak in the upper troposphere and a cooling peak at low-levels. The resulting MCS heating profile is positive at all levels but with a maximum value in

the upper troposphere ("top-heavy" profile).

The convective-stratiform heating (CSH) algorithm has been developed, based on the assumption that the shape of the overall MCS heating profile is determined by the relative amounts of convective and mesoscale heating, which are proportional to the relative amounts of convective and stratiform precipitation (Tao et al. 1993a). An appropriate selection of model-generated convective and stratiform heating profiles, normalized by the convective and stratiform rainfall, from the lookup table is very important for the CSH algorithm (Tao et al. 2000). Schumacher et al. (2004) demonstrated the horizontal variation in the heating profile across the tropics calculated from TRMM PR observations using a method similar to the CSH algorithm, except they used simpler, assumed profiles. In addition, they input their heating profiles into an idealized climate model to determine the response of the large-scale circulation to the heating patterns. However, differences in storm height and distribution of latent heating within a convective or stratiform column were not considered in thse approaches. Recently, Back and Bretherton (2006) suggest that these factors are critically important using reanalysis datasets.

The concept of the spectral approach originates from Austin and Houze (1973) and Houze (1973) in which precipitation top heights (PTHs) observed by surface-based radar data were utilized in estimating the vertical mass transports (proportional to latent heating) by cumulus-scale convection as a function of storm top height. This spectral approach has been extended by Houze and Leary (1976), Leary and Houze (1980), Houze et al. (1980) and Cheng and Houze (1980). Takayabu (2002) applied this spectral concept to obtain a spectral expression of precipitation profiles to examine convective and stratiform rain characteristics as a

function of PTH over the equatorial area (10°N-10°S) observed by the TRMM PR. In her study, nadir data from PR2A25 version 5 (Iguchi et al. 2000) for the period of 1998-1999 were utilized, and convective and stratiform precipitation were separated based on the TRMM PR version 5 2A23 convective-stratiform separation algorithm. Convective rain profiles show near monotonic change with cumulative frequency. Stratiform rain profiles consist of two groups. One group consists of shallow stratiform rain profiles, which are very weak and increase downward. The other group consists of anvil rain profiles, characterized by maximum intensity around the melting level, much less intensity above, and a downward decrease below as indicated in traditional radar observations (e.g., Leary and Houze 1979). Schumacher and Houze (2003b) suggested that since the shallow, isolated echoes represent warm rain processes, they should be classified as convective. After this suggestion of Schumacher and Houze, the spectral plots of Takayabu (2002: Fig. 1) were revised by reclassifying shallow, isolated rain (rain type 15 in product 2A-23) as convective (Shige et al. 2004: Fig. 2).

Based on the results of the spectral precipitation statistics of Takayabu (2002), the Spectral Latent Heating (SLH) algorithm was developed for the TRMM PR in part I of this study (Shige et al. 2004, hereafter Part I). The method uses PR information (i.e., PTH, precipitation rates at the surface and melting level, and rain type) to select the heating profiles in lookup tables. Heating profile lookup tables for the three rain types–convective, shallow stratiform, and anvil rain (deep stratiform with PTH higher than the melting level)–were derived with numerical simulations of tropical cloud systems in TOGA COARE (Tropical Ocean Global Atmosphere Coupled Ocean–Atmosphere Response Experiment – Webster and Lukas 1992)

utilizing a cloud-resolving model (CRM). For convective and shallow stratiform regions, the lookup table is based on the PTH. Considering the sensitivity of the PR, we used a threshold of 0.3 mm h^{-1} to determine the PTH. Properties of the convective and shallow stratiform heating profiles show near-monotonic change with PTH, suggesting that the distribution of latent heating is a strong function of PTH. On the other hand, the PR cannot observe the PTH accurately enough for the anvil regions because of its insensitivity to the small ice-phase hydrometors (Heymsfield et al. 2000). Thus, for the anvil region, the lookup table refers to the precipitation rate at the melting level P_m instead of PTH. The utilization of PTH and P_m provides two distinct advantages for the SLH algorithm. First, the differences in heating profiles between the shallow convective stage and the deep convective stage can be realistically retrieved. Second, heating profiles in the decaying stage with no surface rain can also be retrieved. Preliminary applications of the SLH algorithm using TRMM PR data have been done. Tao et al. (2006) presented latent heating structure for a tropical Pacific Typhoon and a tropical, oceanic MCS estimated by the SLH algorithm. Morita et al. (2006) examined latent heating structure of the Madden-Julian Oscillation (MJO: Madden and Julian 1994) using the SLH estimates. On the other hand, Grecu and Olson (2006) used a procedure similar to the SLH algorithm to assign a heating profile physically consistent with each precipitation profile derived from the the combined TRMM PR–TMI algorithm.

In the subsequent paper (Shige et al. 2007, hereafter Part II), the universality of the lookup table produced from COARE simulations used in the SLH algorithm was examined for its global application to TRMM PR data and improvements were made to the SLH algorithm. In the revised procedure for convective heating

retrieval, the upper-level heating amplitude due to ice processes and lower-level heating amplitude due to liquid water processes are determined separately. In the stratiform region, the heating profile is shifted up or down by matching the melting level in the COARE lookup table with the observed one. The revised SLH algorithm was applied to PR data, and the results compared to Q_1 profiles derived diagnostically from SCSMEX (the 1998 South China Sea Monsoon Experiment) sounding data (Johnson and Ciesielski 2002), where Q_1 is the apparent heat source budget defined in Yanai et al. (1973). Key features of the vertical profiles agree well, particularly the level of maximum heating. Differences of heating profiles between the western Pacific (more "top-heavy") and the Atlantic Ocean (more "bottom-heavy") estimated by the SLH algorithm are also consistent with those from the budget study (Thompson et al. 1979, see a review by Cotton and Anthes 1989). By utilizing the information about precipitation profiles, the SLH algorithm retrieves differences in the shape of convective heating profile between the eastern Pacific and the western Pacific during the cold phase. The differences in the shape of convective heating profiles across the Pacific are consistent with the results from reanalysis datasets (Back and Bretherton 2006).

Large-scale models (i.e., general circulation an climate models) require not only the vertical distribution of Q_1 but also that of Q_2, where Q_2 is the apparent moisture sink budget defined in Yanai et al. (1973). Rajendran et al. (2004) developed a new empirical cumulus parameterization scheme (ECPS), based on a procedure to improve the vertical distribution of heating and moistening over the tropics. The ECPS utilizes observed profiles of Q_1 derived using TMI-CSH algorithm (Tao et al. 1993a) and the European Centre for Medium-Range Weather Forecasts (ECMWF)

analysis based Q_2. Comparisons between short range ECPS forecasts and those with the modified Kuo scheme (Krishnamurti et al. 1983), show a very marked improvement in the skill in ECPS. More improvements may be achieved with ECPS utilizing profiles both Q_1 and Q_2 derived from TRMM data (Rajendran 2005, personal communication). However, none of TRMM heating algorithms estimates Q_2 profiles.

In this study, the SLH algorithm is used to estimate Q_2 profile. First, differences between Q_1 and Q_2 are examined. Second, Q_2 profiles are reconstructed from CRM-simulated parameters (i.e., PTH, precipitation rates at the surface and melting level, and rain type) and compared to the "true" CRM-simulated Q_2 profiles, which are computed directly by the model water vapor equation. Third, the SLH algorithm is applied to PR data and the results compared to Q_2 profiles derived diagnostically from SCSMEX sounding data (Johnson and Ciesielski 2002). It is also applied to PR data for February 1998 and February 1999 to highlight the differences between El Niño–La Niña events.

2. Approach

Figure 1 shows the procedure for refining and validating the SLH algorithm. Due to the scarcity of reliable validation data and difficulties associated with the collocation of validation data and satellite measurements, a consistency check of the SLH algorithm is performed using CRM-simulated precipitation profiles as a proxy for the PR data. The SLH algorithm estimates Q_2 mainly due to precipitation processes, because it is severely limited by the inherent sensitivity of the PR

Fig.1

that can detect only precipitation-sized particles. Hereinafter, Q_2 estimated by the SLH algorithm are represented as Q_{2p} to bring attention to this point. Algorithm-reconstructed Q_{2p} profiles are derived from CRM-simulated precipitation profiles and compared to CRM-simulated "true" Q_2 profiles, which are computed directly from the model water vapor equation. The consistency check is a useful and necessary precondition for the application of the algorithm to actual TRMM PR data. CRM-simulated data from TOGA-COARE, GATE (Global Atmospheric Research Program Atlantic Tropical Experiment – Houze and Betts 1981), SCSMEX and KWAJEX (the 1999 Kwajelin Atoll field experiment – Yuter et al. 2005) are used as a consistency check. Only precipitation over ocean is considered in the current investigation. In this paper, the SLH algorithm is applied to PR data and the results are compared to Q_2 profiles derived diagnostically from SCSMEX sounding data (Johnson and Ciesielski 2002).

The CRM used in this study is the two-dimensional version of the Goddard Cumulus Ensemble (GCE) model and is primarily documented in Tao and Simpson (1993). Recent improvements were presented in Tao (2003) and Tao et al. (2003). The model includes solar and infrared radiative transfer processes, and explicit cloud-radiation interactive processes (Tao et al. 1996). Simulations presented in this study employ a parameterized Kessler-type two-category liquid water scheme (cloud water and rain) and a three-category ice-phase scheme (cloud ice, snow, and graupel) by Rutledge and Hobbs (1984). A "new saturation technique" (Tao et al. 2003), which allows the temperature to change after the water phase before the ice phase is treated, is used. This technique yields far less cloud water and significantly more cloud ice above the freezing level, which is much more in line

with in situ aircraft measurements of there being almost no super cooled cloud water in the anvil (Stith et al. 2002; Heymsfield et al. 2002). Subgrid-scale (turbulent) processes in the GCE model are parameterized using a scheme based on Klemp and Wilhelmson (1978) and Soong and Ogura (1980). The effects of both dry and moist processes on the generation of subgrid-scale kinetic energy have been incorporated in the model. The model domain is 1024 km in the x direction (horizontal) and 22.4 km in the z direction (vertical). The horizontal resolution is 1000 m. The vertical resolution varies from 100 m at the lower boundary to 1000 m at the top of the domain. The time step is 12 s.

In this study, tropical convective systems in TOGA-COARE, GATE, SCSMEX and KWAJEX are simulated with an approach, so-called *cloud ensemble modeling*. In this approach, many clouds of different sizes in various stages of their lifecycles can be present at any model simulation time. Observed large-scale advective tendencies of temperature, moisture, and horizontal momentum are used as the main large-scale forcings that govern the GCE model in a semi-prognostic manner (Soong and Ogura 1980). These are applied uniformly over the model domain with the assumption that the model domain is considerably smaller than the large-scale disturbance. Large-scale advective tendencies for temperature T and specific humidity q are defined as:

$$\left(\frac{\partial T}{\partial t}\right)_{LS} = -\mathbf{v}_{obs}\cdot\nabla T_{obs} - \omega_{obs}\frac{\partial T_{obs}}{\partial p} + \frac{\alpha_{obs}}{C_p}\omega_{obs} \quad (1)$$

$$\left(\frac{\partial q}{\partial t}\right)_{LS} = -\mathbf{v}_{obs}\cdot\nabla q_{obs} - \omega_{obs}\frac{\partial q_{obs}}{\partial p} \quad (2)$$

and were derived from sounding networks deployed during TOGA COARE, GATE, SCSMEX and KWAJEX. Here $\mathbf{v}$ is the horizontal wind vector, ω the vertical pres-

sure velocity, α the specific volume, and C_p the heat capacity at constant pressure.

Since accurate calculations of the large-scale horizontal momentum forcing terms are difficult to obtain from observations in the Tropics (Soong and Tao 1984), the terms are instead replaced by a nudging term:

$$\left(\frac{\partial \mathbf{v}}{\partial t}\right)_{LS} = -\frac{\bar{\mathbf{v}} - \mathbf{v}_{obs}}{\tau} \tag{3}$$

where $\bar{\mathbf{v}}$ is the model domain averaged horizontal velocity, $\mathbf{v}_{obs}$ the observed large-scale horizontal vector over the sounding networks, and τ the specified adjustment time scale of six hours. This method constrains the domain-averaged horizontal velocities to follow the observed values, and thereby provides a simple means in controlling the cloud system dynamics by the large-scale momentum and shear. Cyclic lateral boundary conditions are incorporated to ensure that there is no additional heat and moisture forcing inside the domain other than the imposed large-scale forcing.

The accuracy of the convective-stratiform separation affects the inference of the vertical distribution of heating and moistening. The TRMM PR rain-type classifications, in which bright band identification is very important, cannot be directly applied to GCE outputs (Awaka et al. 1996). The microphysical schemes utilized in CRMs (e.g., Lin et al. 1983; Rutledge and Hobbs 1984) typically do not contain an explicit description of the partially melted precipitation particles that lead to a bright band of enhanced radar reflectivity. Thus, the GCE convective and stratiform separation method (Lang et al. 2003) is used with some modifications done in Part I to maintain the consistency with the TRMM PR rain-type classification.

3. Heat and moisture budgets

In diagnostic studies (Yanai et al. 1973; Yanai and Johnson 1993), it is customary to define the *apparent heat source* Q_1 and the *apparent moisture sink* Q_2 of a large-scale system by averaging horizontally the thermodynamic and water vapor equations as

$$Q_1 = \bar{\pi}\left[\frac{\partial \bar{\theta}}{\partial t} + \bar{\mathbf{V}} \cdot \nabla \bar{\theta} + \bar{w}\frac{\partial \bar{\theta}}{\partial z}\right] \tag{4}$$

$$Q_2 = -\frac{L_v}{C_p}\left[\frac{\partial \bar{q}_v}{\partial t} + \bar{\mathbf{V}} \cdot \nabla \bar{q}_v + \bar{w}\frac{\partial \bar{q}_v}{\partial z}\right] \tag{5}$$

where $\pi = (p/P_{00})^{R/Cp}$ is the nondimensional pressure, P_{00} the reference pressure (1000 mb), C_p the specific heat of dry air at constant pressure, and R the gas constant for dry air.

Q_1 and Q_2 can be directly related to the contributions of cloud effects, which can be explicitly estimated by CRMs as:

$$Q_1 = \bar{\pi}\left[-\frac{1}{\bar{\rho}}\frac{\partial \bar{\rho}\overline{w'\theta'}}{\partial z} - \overline{\mathbf{v}' \cdot \nabla \theta'} + \bar{D}_\theta\right] + \overline{LH} + \bar{Q}_R, \tag{6}$$

$$Q_2 = \frac{L_v}{C_p}\left[\frac{1}{\bar{\rho}}\frac{\partial \bar{\rho}\overline{w'q'}_v}{\partial z} - \overline{\mathbf{v}' \cdot \nabla q'_v} + \bar{D}_{q_v}\right] + \overline{NC}. \tag{7}$$

The overbars denote horizontal averages; the primes indicate deviations from the horizontal averages. $\bar{\rho}$ is the air density, and Q_R the cooling/heating rate associated with radiative processes. The subgrid-scale (smaller than the cloud scale) diffusion are represented by D_θ and D_{q_v} that are usually small compared to other terms above the boundary layer (Soong and Tao 1980). The term LH and NC are the

net latent heating and the net condensation due to the phase change of water:

$$LH = \frac{L_v}{C_p}(c - e) + \frac{L_f}{C_p}(f - m) + \frac{L_s}{C_p}(d - s), \tag{8}$$

$$NC = \frac{L_v}{C_p}(c - e + d - s). \tag{9}$$

L_v, L_f and L_s are the latent heats of vaporization, fusion and sublimation, respectively. Variables c, e, d and s stand for the rates of condensation of cloud droplets, evaporation of cloud droplets and raindrops, freezing of cloud droplets and raindrops, melting of ice crystals, snow and graupel, deposition of ice crystals and sublimation of all ice hydrometeors, respectively. These processes are not directly detectable with remote sensing (or for that matter, with *in situ* measurements). Thus, heating and moistening retrieval schemes depend heavily on the use of CRM. The first terms on the right-hand side of Eqs (6) and (7) are the vertical eddy heat and moisture flux convergences from upward and downward cloud-scale motions, respectively. The second term are the horizontal eddy heat and moisture flux convergences, respectively.

We accumulate Q_1 and Q_2 over a period of 5 minutes for each data sampling, since accumulation over long periods are inadequate for growing convective cells (Shige and Satomura 2000: Fig. 4a) and moving convective systems. Additional sensitivity tests with periods of 1 minute and 2 minutes indicate that there are more quantitative differences in convective and stratiform components of Q_2 than those of Q_1. In this study, the two-dimensional version of the GCE model was used. Real clouds and cloud systems are three-dimensional. Grabowski et al. (1998) and Donner et al. (1999) found larger temporal variability in the two-dimensional simulation than in the three-dimensional simulation. Thus, the sensitivity of Q_2 in

convective and stratiform regions to accmulated time might be smaller in the three-dimensional simulation than in the two-dimensional simulation, but it is beyond the scope of this study. Hereafter Q_1 and Q_2 accumulated over a period of 5 minutes for each data sampling are represented as instantaneous Q_1 and Q_2 to maintain consistency with Part I and II.

Figures 2a–f show GCE-simulated average profiles of heat budget [LH, $Q_1 - Q_R$ (hereinafter Q_{1R}) without and with horizontal eddy heat flux] and moisture budget [NC, Q_2 without and with horizontal eddy heat flux] for the TOGA COARE (19–26 December 1992) case, respectively. The difference between LH and NC around 4.4 km is large (Figs 2a, d). The maximum of NC around 4.4 km can be explained by a decrease of saturation water vapor mixing ratio, which is due to the melting cooling (Guichard et al. 1997). It is also evident that the NC magnitudes are smaller than the LH magnitude above 6 km, because freezing is included in LH (Eq. (8)), but not in NC (Eq. (9)).

Fig.2

The profile of Q_{1R} for the total region (Fig. 2b) is close to that of LH for the total region (Fig. 2a) except the melting level where the vertical eddy heat flux convergence compensates for the distinct LH cooling due to the melting for the total region (Sui et al. 1994; Shie et al. 2003). On the other hand, the profile of Q_2 for the total region (Fig. 2e) does not follow that of NC for the total region (Fig. 2d) and has a more complicated shape. The vertical eddy moisture flux convergence is a major contributor to the Q_2 while the contribution to the Q_{1R} budget by the vertical eddy heat flux convergence is minor, as noted by previous studies (Soong and Tao 1980; Tao and Soong 1986; Lafore et al. 1988; Chong and Hauser 1990; Simpson and Tao 1993; Tao et al. 1993b; Caniaux et al. 1994; Guichard et al. 1997). This

difference is explained by the fact that the vertical gradient of the mean water vapor is larger than that of the mean potential temperature.

The horizontal eddy heat and moisture flux convergences have been neglected in most of the previous studies. Neglecting the horizontal eddy heat and moisture flux convergences is appropriate for Q_{1R} and Q_2 for the total region because differences between profiles of Q_{1R} and Q_2 without and with horizontal eddy heat flux are negligible. However, as discussed in Part II, there are the differences between profiles of Q_{1R} without and with horizontal eddy heat flux in the convective and stratiform regions (Figs 2b, c), and thus horizontal eddy heat flux should not be neglected. Larger differences between profiles of Q_2 without and with horizontal eddy moisture flux in the convective and stratiform regions can be found (Figs 2e, f). Larger differences of Q_2 than Q_{1R} can be attributed to the greater horizontal variability of moisture than temperature.

Lafore et al. (1988) and Caniaux et al. (1994) argued that the double-peak structure in Q_2 often seen in tropical budget studies (Reed and Recker 1971; Yanai et al. 1973; Johnson 1976) is a result of midtropospheric moistening by vertical eddy moisture convergence in the convective region, while Johnson (1984) explained this structure as a consequence of the combined but vertically separated drying effects of convective and stratiform regions. Although the TOGA-COARE IFA (Intensive Flux Array) Q_2 profile does not exhibit a prominent double-peak structure as shown in Figs 2f, there are times when the TOGA-COARE IFA Q_2 profiles do resemble those obtained by the previous study (Johnson and Lin 1997). An example is during a period of heavy rainfall on 11-17 December (Fig. 3; see also Fig. 3 of Johnson and Lin 1997). A double peak in Q_2 is present (though not

Fig.3

very pronounced). Profiles of Q_2 without horizontal eddy heat flux in the convective and stratiform regions (Figs 2b) are in good agreement with those of Q_2 in the convective and stratiform regions simulated by Caniaux et al. (1994: their Fig. 22b). Caniaux et al. (1994) neglected horizontal eddy moisture flux convergence, because it is one order of magnitude smaller than NC and vertical eddy moisture flux convergence. This is true for the total region, but not for the convective and stratiform regions. The horizontal eddy moisture flux convergence compensates midtropospheric moistening by vertical eddy moisture convergence in the convective regions during this period (Fig. 3c), as well as the period of heavy rainfall on 19-26 December (Fig. 2f). From our results, the double-peak structure is likely explained as a consequence of the combined but vertically separated drying effects of convective and stratiform regions. It should be noted that Lafore et al. (1988) and Caniaux et al. (1994) examined a tropical continental squall line. Updrafts associated with tropical continental cases are expected to be stronger than those associated with tropical oceanic ones. Thus, even if the horizontal eddy moisture flux convergence is included, their results might be different from ours.

The SLH algorithm estimates Q_{1R} and Q_2 mainly due to precipitation processes (Q_{1Rp} and Q_{2p}), because it is severely limited by the inherent sensitivity of the PR that can detect only precipitation-sized particles. However, it is noticed in Figs 2 and 3 that the Q_2 in the nonprecipitating region is the same order as that in the stratiform region, while the Q_{1R} profile in the nonprecipitating region is negligible. Thus, we cannot expect that differences between Q_{2p} and Q_2 are as small as those between Q_{1Rp} and Q_{1R}.

4. Algorithm

a. *Construction of lookup tables*

The Q_{2p} profile lookup tables have been constructed for the three rain types; convective, shallow stratiform, and deep stratiform with and without surface rain (Fig. 4). For construction of lookup tables, the GCE-simulated precipitation profiles and corresponding Q_{2p} profiles from the four sub-periods of 9-day durations (10-18 December 1992, 27 December 1992 - 4 January 1993, 9-17 February 1993, and 18-26 February 1993) are used.

Fig.4

Figure 4a shows the lookup table for convective rain. The GCE-simulated precipitation profiles with 0.3 mm h^{-1} precipitation top threshold and corresponding Q_{2p} profiles are accumulated and averaged for each PTH with model grid intervals. Properties of convective Q_{2p} profiles show less monotonic changes with PTH than Q_{1Rp} do (Part II: Fig. 5a) because contribution of eddy fluxes is larger in Q_{2p} than in Q_{1Rp}.

As for the stratiform precipitation, the GCE-simulated precipitation profiles with 0.3 mm h^{-1} precipitation top threshold and corresponding Q_{2p} profiles are also averaged for each PTH (Fig. 4b). However, as mentioned earlier, we cannot expect the PR to retrieve the small ice-phase precipitation, and observe the PTH accurately enough in the upper-level regions of the anvils where small ice-phase hydrometors dominate as mentioned earlier. Therefore, only the stratiform Q_{2p} profiles with PTH lower than 4.4 km (shown in Fig. 4b), characterized by moistening around PTH levels, are used as the shallow stratiform heating profile lookup table

for the SLH algorithm.

Figure 4c shows lookup table for anvil (deep stratiform with PTH higher than the melting level) rain. PR can measure the precipitation rate at the melting level as well as surface-based radar (*e.g.* Leary and Houze 1979), although it cannot observe the PTH accurately enough in the upper-level regions of the anvils. Thus, for the anvil region, the lookup table refers to the precipitation rate at the melting level P_m instead of PTH (Part I). The anvil profiles with PTH higher than the melting level are characterized by upper-level drying and lower-level moistening, which is also found in observations (*e.g.* Johnson and Young 1983). The upper level drying in these anvil regions is largely due to condensation and deposition, while the lower-level moistening is largely due to evaporation of raindrops.

b. *Procedure of Q_{2p} retrieval*

Procedure of Q_{2p} retrieval is the same as that of heating retrieval (Part I, II) except for using the Q_{2p} tables (Fig. 4). The SLH algorithm utilizes the observed information on precipitation type (convective or stratiform), PTH, P_s, and P_m. The convective region is then separated into a shallower convective region and a deeper convective region. On the other hand, the stratiform region is separated into a shallow stratiform region and an anvil region based on the PTH in comparison with the melting level. The algorithm then derives Q_{p2} profiles based on the following procedure for each of the four regions (Fig. 5).

Fig.5

For shallower convective regions as well as shallow stratiform regions, a Q_{2p} profile corresponding to the PTH is selected in the convective Q_{2p} profile (Fig. 4a)

and PTH-based shallow stratiform Q_{2p} profile (Fig. 4b) lookup tables, respectively. The amplitude is determined by

$$Q(z) = \frac{\tilde{Q}(z)}{\tilde{P}_s} \cdot P_s. \tag{10}$$

For deeper convective regions, the upper-level drying due to ice processes is determined by

$$Q(z)_{high} = \frac{\tilde{Q}_{high}(z)}{\tilde{P}_f} \cdot P_f. \tag{11}$$

where P_f is the precipitation rate at the level separating upper-level drying from lower-level drying. Likewise, the lower-level drying due to liquid water processes is determined by

$$Q(z)_{low} = \frac{\tilde{Q}_{low}(z)}{\tilde{P}_s} \cdot P_s. \tag{12}$$

For anvil regions with PTH higher than the melting level, on the other hand, the Q_{2p} profile corresponding to P_m is selected in the anvil Q_{2p} profile lookup table (Fig. 4c). The upper-level drying amplitude is then determined by

$$Q_{high}(z) = \frac{\tilde{Q}_{high}(z)}{\tilde{P}_m} \cdot P_m. \tag{13}$$

Evaporative moistening rate below the melting level in the anvil regions is proportional to the reduction of precipitation profile toward the surface from the melting level. The downward decrease of the intensity of anvil rain below the melting layer has been statistically indicated in the PR observation (see Fig. 2 of Takayabu, 2002) as well as in case studies of traditional radar observations (e.g. Leary and Houze 1979). Thus, the algorithm computes the lower-level moistening amplitude Q_{low} as a function of the difference of rainfall rate between the surface and the

melting level $P_m - P_s$:

$$Q_{low}(z) = \frac{\tilde{Q}_{low}(z)}{\tilde{P}_m - \tilde{P}_s} \cdot (P_m - P_s) \tag{14}$$

The above procedure allows us to estimate the Q_{2p} profiles in the anvil regions both with and without surface precipitation. The Q_{2p} profile is shifted up or down by matching the melting level of the COARE lookup table with the observed one.

5. Consistency check

a. *Time averaged profiles*

Four eight-day periods from TOGA-COARE (19–26 December 1992), GATE (Sep 1–8 1974), SCSMEX (Jun 2–9 1998) and KWAJEX (Sep 6–13 1999) are used for a consistency check of the SLH algorithm, as shown in Fig. 6. For each period, Q_{2p} profiles were reconstructed using the simulated parameters (i.e. PTH, convective/stratiform characteristics, P_s, and P_m) as input. The algorithm-reconstructed Q_{2p} profiles from the GCE-simulated precipitation profiles are compared with GCE-simulated true Q_2 profiles for the convective, stratiform, non-precipitating and total regions.

Fig.6

For the COARE case, the SLH algorithm with the COARE lookup table produces good agreement between the SLH-reconstructed Q_{2p} and GCE-simulated Q_2 profiles for convective and stratiform regions (Fig. 6a). The reconstructed total Q_{2p} profile is in good agreement with the model except for lowest-levels where moistening due to non-precipitating processes is dominant.

For the GATE case, the COARE lookup table results in less agreement between the SLH-reconstructed and GCE-simulated profiles for convective and stratiform regions (Fig. 6b). The SLH-reconstructed drying at z = 1–3 km is weaker than the GCE-simulated for the convective region, while the SLH-reconstructed moistening at z = 1–3 km is weaker than the GCE-simulated for the stratiform region. In spite of compensating errors at z = 1–3 km from each component (convective and stratiform), the SLH-reconstructed drying at z = 2–6 km is stronger than the GCE-simulated for the total region. This discrepancy is mostly explained by moistening for non-precipitating region that SLH cannot reconstruct.

The COARE lookup table produces good agreement between reconstructed Q_{2p} and simulated Q_2 profiles for the SCSMEX convective and stratiform regions (Fig. 6c). In addition to good agreement for the convective and stratiform regions, contribution of non-precipitating region to the SCSMEX total Q_2 profile is small, leading good agreement reconstructed Q_{2p} and simulated Q_2 profiles for the SCSMEX total region.

For the KWAJEX case, the SLH-reconstructed drying below z = 4 km is weaker than the GCE-simulated for the convective Q_2 profiles, and while the SLH-reconstructed moistening below z = 4 km is weaker than the GCE-simulated for the stratiform Q_2 profiles, similar to the GATE case. Because of compensating errors below z = 4 km from each component (convective and stratiform), the reconstructed total Q_2 profile is in good agreement with the model except for lowest-levels where moistening due to non-precipitating processes is dominant.

The differences between the SLH-reconstructed Q_{2p} and GCE-simulated Q_2 shown here are larger than those between the SLH-reconstructed Q_{1Rp} and GCE-

simulated Q_{1R} (Part II: Fig. 9). This is because the Q_2 profiles are noisier than those of Q_{1R} due to much more contribution of eddy fluxes. The SLH algorithm cannot estimate the effect (moistening) of non-precipitating area, leading to a discrepancy with the GCE results. Nevertheless, the SLH-reconstructed total Q_{2p} profiles are in good agreement with the GCE-simulated ones, espcially for the case where contribution of non-precipitating region to the Q_2 budget is small.

b. *Error estimation*

In the SLH algorithm, lookup tables are constructed based on the assumption that heating profiles correspond statistically to precipitation profiles or precipitation parameters (i.e., PTH, P_m). However, the instantaneous grid cell relationship between precipitation profiles and Q_{2p} is somewhat ambiguous. Part II performed a preliminary evaluation of the horizontally averaged estimates and found that horizontal averaging over ~30 km width was required to reduce random errors in the SLH-reconstructed heating profiles to acceptable levels.

Following Part II, a preliminary evaluation of the horizontally-averaged estimates of Q_{2p} for the COARE, GATE, SCSMEX and KWAJEX periods used in the consistency check is performed. Q_{2p} profiles were reconstructed grid by grid for each 8-day periods using the simulated parameters as input. Then, the differences between the reconstructed Q_{p2} profiles and the simulated Q_2 were examined statistically to see the errors in the instantaneous grid cell estimates using the table method. Larger root-mean-square (rms) errors were found for Q_{2p} than with Q_{1Rp} (Part II: Fig. 10). While the rms errors of Q_{1Rp} at the PR foot-print scale (4 km)

are smaller than 16 K^2 h^{-2}, those of Q_{2p} are much larger than 16 K^2 h^{-2}. Larger contribution of eddy fluxes in the Q_{2p} budget than in the Q_{1Rp} budget is a major reason. Averaging over ~60 km in width reduces the rms to about 1 K^2 h^{-2}. From these results, averaging over ~60 km in width is recommended in order to use the SLH algorithm estimates of Q_2 quantitatively.

Fig.7

6. PR applications

In this section, the revised SLH algorithm is applied to precipitation profiles from version 6 of the TRMM PR 2A25 data set, which is instantaneous and at footprint-scale (i.e., a level-2 product). Recently, Shige et al. (2006) investigated the consistency between TMI-observed brightness temperatures (TBs) and those simulated from PR2A25 V5 and V6 rain profiles using a radiative transfer model. They showed that simulated TBs from PR V6 exhibits better agreement with observed ones than those from PR V5, implying the algorithm improvements. Bright-band height estimates from version 6 of TRMM PR 3A25, gridded five degree spatial resolution monthly composite of instantaneous and footprint-scale data (PR 2A25), are also used as the melting levels.

a. *Comparison of Q_2 profiles over the SCSMEX NESA region*

In Part II, the accuracy of the SLH-retrieved heating was evaluated by comparing with a rawinsonde-based analysis of diabatic heating for the SCSMEX NESA derived by Johnson and Ciesielski (2002). Key features of the vertical profiles

Fig.8

agree well, particularly the level of maximum heating. Magagi and Barros (2004) and Grecu and Olson (2006) also compared their results against heating estimates over the SCSMEX NESA. Here, the accuracy of the SLH-retrieved Q_{2p} are evaluated by comparing with a rawinsonde-based analysis of Q_2 for the SCSMEX NESA derived by Johnson and Ciesielski (2002).

Figure 8 shows a comparison between SLH-retrieved Q_{2p} from version 6 of the TRMM PR data sets and sounding-based Q_2 during the campaign's most convectively active period (May 15 – Jun 20 1998). Mapes et al. (2003) suggested that averages of about 30 days reduce sampling errors in the rainfall rate estimate (proportional to integrated Q_1 or Q_2) to 10% for the SCSMEX NESA. There is good agreement in several key features of the vertical profiles. It is evident from Fig. 8 that the Q_{2p} drying magnitudes are smaller than the sounding-derived magnitudes in the upper troposphere. The Q_{1Rp} heating magnitudes were also smaller than the sounding-derived magnitudes in the upper troposphere (Part II: Fig. 11). The SLH algorithm is severely limited by the inherent sensitivity of the PR that can detect only precipitation-sized particles. During the growing phase of a congestus cloud, cloud top and radar-echo top may correlate well (Kingsmill and Wakimoto 1991). However, during the decaying phase of a cumulonimbus cloud and in stratiform regions, the two tops may differ significantly, leading to underestimate of drying in the upper troposphere. Therefore, measurements from other sensors [e.g., VIRS (Visible and Infrared Scanner)] will have to be integrated to obtain a more accurate estimation of moistening profiles, but it is beyond the scope of this study.

b. *El Niño–La Niña*

Figures 9a,b show the monthly mean surface rainfall (mm day^{-1}) for February 1998 and February 1999, respectively. Drying/moistening structures over the six oceanic regions (western Pacific, central Pacific, east Pacific, south Pacific, Indian Ocean and Atlantic Ocean) shown in Fig. 9 will be examined and compared. Heating structures over the same regions were examined in Part II.

Fig.9

Figures 10 and 11 show the monthly mean convective, stratiform and total Q_{2p} profiles derived from the SLH algorithm for six locations over the tropical oceans for February of 1998 and February of 1999, respectively. Also total Q_{1Rp} profiles derived from the SLH algorithm are shown.

Fig.10

Fig.11

A maximum at low-levels (~0.5 km) is found in the SLH-estimated total Q_{2p} profile over the western Pacific for February 1998 (Fig. 10a). This low-level maximum in the SLH-estimated total Q_{2p} profile comes from the SLH-estimated convective Q_{2p} profile with a low-level maximum, reflecting the abundance of shallow convection. Diagnostic budget studies over west Pacific regions (Reed and Recker 1971; Nitta 1972; Yanai et al. 1973; Lin and Johnson 1996) indicate a double-peak structure with a minimum near 4 km. While the SLH-estimated mean Q_{2p} profile for February 1999 show a minimum near 4 km (tough not very pronounced), the SLH-estimated mean Q_{2p} profile with the low-level maximum for February 1998 does not resemble those determined from the diagnostic budget studies. It should be noted that diagnostic budget studies over the western Pacific do not contain periods corresponding to the warm phases of ENSO, except for two months out of the period from March to July of 1958 in Nitta (1972). The SLH-estimated mean Q_{2p}

profile for February 1998 resembles the mean Q_2 profile with a lower-level maximum over the GATE region (Nitta 1978; Thompson et al. 1979), which is due to the different cloud population and lower SSTs in the GATE region. Deep convection over the western Pacific is suppressed during the warm phase of ENSO (February 1998) relative to the cold phase (February 1999) due to lower sea surface temperatures. Thus, the difference in the SLH-estimated mean Q_{2p} profile between February 1998 and February 1999 may be reasonable.

There are dramatic differences in total Q_{2p} profiles over the central and eastern Pacific between the 1998 El Niño event and the 1999 La Niña event. First, these differences can be attributed to those in stratiform rain fraction (Schumacher and Houze 2003a). Second, the shape of convective Q_{2p} profiles also affect total Q_{2p} profiles. The convective Q_{2p} profiles are shallower during La Niña than El Niño.

Part II pointed out that the SLH-estimated heating profile over the south Pacific for February 1998 is very similar to the vertical distribution of heating during the undisturbed BOMEX (the Barbados Oceanographic and Meteorological Experiment) period in the trade wind belts (Nitta and Esbensen 1974) and that during episodic trade wind regimes over the western Pacific (Johnson and Lin 1997). On the other hand, the SLH-estimated Q_{2p} profile with low-level drying over the south Pacific for February 1998 is not similar to the vertical distribution of Q_2 with low-level moistening during the undisturbed BOMEX and that during episodic trade wind regimes over the western Pacific. Possible reason for the differences is that contribution of non-precipitating region to the Q_2 budget which SLH cannot retrieve is large. Another reason is that there is larger spatial variability in Q_2 profiles than in Q_1 profiles. For example, Lin and Johnson (1996) indicated that although the

heating profiles over different regions of the western Pacific warm Pool are similar to one another, the drying/moistening profiles are significantly different.

The SLH-estimated Q_{2p} profiles over the Atlantic Ocean for February 1998 and February 1999 resemble the mean Q_2 profile with a lower-level maximum that was determined from a diagnostic budget study during GATE (Nitta 1978; Thompson et al. 1979) and simulated by the GCE model (see Fig. 6b). Thus, it is shown that the SLH algorithm can estimate differences of Q_{2p} between the western Pacific and the Atlantic Ocean as well as those of Q_1, which are also consistent with the results from the budget study (Thompson et al. 1979, see a review by Cotton and Anthes 1989).

Over the Indian Ocean, even indirect validation using the results of diagnostic studies for different years is difficult because of the lack of observations*. The SLH-estimated Q_{2p} profile shape over the Indian Ocean for February 1998 resemble that over the western Pacific for February 1999, while that over the Indian Ocean for February 1999 resemble that over the Atlantic Ocean. The differences in the SLH-estimated Q_{2p} over the Indian Ocean between February 1998 and February 1999 are consistent with those in the SLH-estimated Q_{1R} over the Indian Ocean between February 1998 and February 1999.

*Nitta (1980) did preliminary budget computations over the bay of Bengal for a very short time (three-day period).

c. *Variability of Q_{2p} profile*

The average profiles shown in Figs. 10 and 11 may not be very representative, because there are large spatial and temporal variabilities in rainfall over a larger region such as those selected in Fig. 9. Following Part II, we used contoured-frequency-by-altitude diagrams (CFADs; Yuter and Houze 1995) in order to provide actual variability of drying/moistening profile shapes.

Fig.12

Fig.13

Many of the negative values in the low to middle troposphere in Fig. 12a-e and Fig. 13a, b and d are associated with evaporation in the stratiform region, suggesting large variability in stratiform rain fraction over the regions. The distinct peak in the frequency of drying at levels below 2 km is also evident for all six geographic areas for both February 1998 and February 1999 in the CFADs (Figs. 12 and 13), corresponding to a drying peak at lowest-levels seen in the mean convective heating profiles (Figs. 10 and 11). It is inferred from the convective Q_{2p}-profile lookup table (Fig. 4a) that shallow convection with PTHs lower than 4 km accounts for this distinct peak.

The CFADs of IFA-mean Q_1 and Q_2 during TOGA COARE have been shown by Johnson and Ciesielski (2000: Fig. 3). Direct comparison of the CFADs shown in Figs 12 and 13 against those in Johnson and Ciesielski (2000) cannot be done, because the CFADs shown in Figs 12 and 13 are derived form monthly mean Q_{2p} profiles at 0.5^o resolution. Still, there is a striking difference. In the CFAD of Q_2 in Johnson and Ciesielski (2000), there is some contribution to negative values of Q_2 in the lowest 2 km from shallow cumulus clouds and subcloud-layer eddies during non-precipitating periods of the TOGA-COARE IOP (Johnson and

Lin 1997). On the other hand, there is almost no contribution to negative values of Q_{2p} in the lowest 2 km from shallow cumulus clouds and subcloud-layer eddies, although there is some contribution to negative values of Q_{2p} in the lowest 2 km from stratiform rain. Again, the SLH algorithm cannot retrieve moistening for non-precipitating regiondue to the sensitivity of the PR.

7. Summary and future work

In this study, the SLH algorithm was used to estimate Q_2 profiles from PR data together with Q_{1R} profiles. There are two differences between Q_{1R} and Q_2. First, the eddy moisture flux convergence is a major contributor to the Q_2 while the contribution to the Q_{1R} budget by the eddy heat flux convergence is minor. Second, the Q_2 in the nonprecipitating region is the same order as that in the stratiform region, while the Q_{1R} profile in the nonprecipitating region is negligible. These two factors lead to larger errors of Q_2 than Q_{1R}.

The Q_{2p} profiles were reconstructed from CRM-simulated parameters (i.e. PTH, precipitation rate at the melting level, rain rate and type) with the COARE table and compared then to CRM-simulated "true" Q_2 profiles, which were computed directly from the model water vapor equation. COARE, GATE, SCSMEX, and KWAJEX periods were used for the consistency check. The consistency check indicates that discrepancies between the SLH-reconstructed Q_{2p} and GCE-simulated Q_2 profiles, especially at low levels, are larger than those between the SLH-reconstructed Q_{1Rp} and GCE-simulated Q_{1R} profiles. Larger discrepancies in Q_{2p} at low levels are due to moistening for non-precipitating region that SLH cannot reconstruct.

The SLH algorithm was applied to PR data, and the results compared to Q_2 profiles derived diagnostically from SCSMEX sounding data. Although discrepancies between the SLH-retrieved and sounding-based profiles for Q_2 are larger than those for Q_{1R}, key features of the vertical profiles agree well. The Q_{2p} drying magnitudes are smaller than the sounding-derived magnitudes in the upper troposphere. This is because the SLH algorithm is severely limited by the inherent sensitivity of the PR that can detect only precipitation-sized particles. During the decaying phase of a cumulonimbus cloud and in stratiform regions, cloud top and radar-echo top may differ significantly, leading to underestimate of drying in the upper troposphere.

The SLH algorithm was also applied to PR data for February 1998 (El Niño) and February 1999 (La Niña). The differences in the SLH-estimated Q_2 between February 1998 and February 1999 are consistent with those in the SLH-estimated Q_{1R} between February 1998 and February 1999. It is shown that the SLH algorithm can estimate differences of Q_{2p} between the western Pacific and the Atlantic Ocean as well as those of Q_{1p}, which are consistent with the results from the budget study (Thompson et al. 1979, see a review by Cotton and Anthes 1989).

Although the SLH-estimated heating profile over the south Pacific for February 1998 is very similar to the vertical distribution of heating during the undisturbed BOMEX period in the trade wind belts (Nitta and Esbensen 1974) and that during episodic trade wind regimes over the western Pacific (Johnson and Lin 1997), the SLH-estimated Q_{2p} profile with low-level drying over the south Pacific for February 1998 is not similar to the vertical distribution of Q_2 with low-level moistening during the undisturbed BOMEX and that during episodic trade wind regimes over the

western Pacific. Possible reason is that SLH cannot retrieve moistening for non-precipitating region due to the sensitivity of the PR. Measurements from other sensors (e.g., VIRS) will have to be integrated to obtain a more accurate estimation of moistening profiles.

In this study, the two-dimensional version of the GCE model was used. Real clouds and cloud systems are three-dimensional. The availability of exponentially increasing computer capabilities has resulted in three-dimensional CRM simulations for multiday periods with large horizontal domains becoming increasing prevalent (e.g., Grabowski et al. 1998, Donner et al. 1999). Grabowski et al. (1998) showed the similarity in statistical aspects between the two- and three-dimensional CRM simulations. The reason for the similarity between the two- and three-dimensional CRM simulations is that the same observed large-scale advective tendencies temperature and water vapor mixing ratio were used as the main forcing (Tao et al. 1987). However, there are notable differences between the two- and three-dimensional CRM simulations. Larger temporal variability in the two-dimensional simulation than in the three-dimensional simulation was found in Grabowski et al. (1998) and Donner et al. (1999). Tao et al. (2000, 2003) pointed out that the GCE three-dimensional model simulated water vapor (Q_2) budget is in better agreement with observations in the lower-troposphere than its two-dimensional counterpart. We are now performing the three-dimensional CRM simulations in order to compare look-up tables from the two- and three-dimensional CRM simulations.

Acknowledgments.

This study is supported by the Japan Aerospace Exploration Agency/Earth Observation Research Center (JAXA/EORC) TRMM project. He is also supported by the fund of JST Corporation - Core Research for Evolution Science and Technology (CREST). He thank Prof. Richard Johnson of Colorado State University for his comments. Yukari N. Takayabu would like to express her hearty gratitude to the late Prof. Tsuyoshi Nitta for motivating her to develop the latent heating algorithm utilizing TRMM PR data. W.-K. Tao is mainly supported by the NASA headquarters Atmospheric Dynamics and Thermodynamics Program and the NASA TRMM. The TRMM products were provided by JAXA. The Grid Analysis and Display System (GrADS) package was utilized for the figures.

References

Austin, P. M. and R. A. Houze Jr., 1973: A technique for computing vertical transports by precipitating cumuli. *J. Atmos. Sci.*, **30**, 1100–1111.

Awaka, J., T. Iguchi, and K. Okamoto, 1998: Early results on rain type classification by the Tropical Rainfall Measuring Mission (TRMM) precipitation radar. *Proc. 8th URSI Commission F Open Symp.*, URSI, Aveiro, Portugal, 143–146.

Awaka, J., H. Kumagai, T. Iguchi, and K. Okamoto, 1996: Development of an algorithm for classifying rain types (in Japanese). *J. Commun. Res. Lab.*, **42**, 325–337.

Back, L. E. and C. S. Bretherton, 2006: Geographic variability in the export of moist static energy and vertical motion profiles in the tropical Pacific. *Geophys. Res. Lett.*, **33**, L17810, doi:10.1029/2006GL026672.

Caniaux, G., J.-L. Redelsperger, and J.-P. Lafore, 1994: A numerical study of the stratiform region of a fast-moving squall line. Part I: General description and water and heat budgets. *J. Atmos. Sci.*, **51**, 2046–2074.

Cheng, C. P. and R. A. Houze Jr., 1980: Sensitivity of diagnosed convective fluxes to model assumptions. *J. Atmos. Sci.*, **37**, 774–783.

Chong, M. and D. Hauser, 1990: A tropical squall line observed during the COPT81 experiment in West Africa. Part III: Heat and moisture budgets. *Mon. Wea. Rev.*, **118**, 1696–1706.

Cotton, W. R. and R. A. Anthes, 1989: *Storm and Cloud Dynamics*. Academic Press, 883pp.

Donner, L. J., C. J. Seman, and R. S. Hemler, 1999: Three-dimensional cloud-system modeling of GATE convection. *J. Atmos. Sci.*, **56**, 1885–1912.

Grabowski, W. W., X. Wu, M. W. Moncrieff, and W. D. Hall, 1998: Cloud-resolving modeling of tropical cloud systems during Phase III of GATE. Part II: Effects of resolution and the third spatial dimension. *J. Atmos. Sci.*, **55**, 3264–3282.

Grecu, M. and W. S. Olson, 2006: Bayesian estimation of precipitation from satellite passive microwave observations using combined radar–radiometer retrievals. *J. Appl. Meteor. Climatol.*, **45**, 416–433.

Guichard, F., J.-P. Lafore, and J.-L. Redelsperger, 1997: Thermodynamical impact and internal structure of a tropical convective cloud system. *Quart. J. Roy. Meteor. Soc.*, **123**, 2297–2324.

Heymsfield, A., A. Bansemer, P. R. Field, S. L. Durden, J. L. Stith, J. E. Dye, W. Hall, and C. A. Grainger, 2002: Observations and parameterizations of particle size distributions in deep tropical cirrus and stratiform precipitating clouds: Results from in situ observations in TRMM field campaigns. *J. Atmos. Sci.*, **59**, 3457–3491.

Heymsfield, G. M., B. Geerts, and L. Tian, 2000: TRMM precipitation radar reflectivity profiles as compared with high-resolution airborne and ground-based radar measurements. *J. Appl. Meteor.*, **39**, 2080–2102.

Houze, R. A., Jr., 1973: A climatological study of vertical transports by cumulus-scale convection. *J. Atmos. Sci.*, **30**, 1112–1123.

— 1982: Cloud clusters and large-scale vertical motions in the tropics. *J. Meteor. Soc. Japan*, **60**, 396–410.

Houze, R. A., Jr. and A. K. Betts, 1981: Convection in GATE. *Rev. Geophys. Space Phys.*, **19**, 541–576.

Houze, R. A., Jr., C.-P. Cheng, C. A. Leary, and J. F. Gamache, 1980: Diagnosis of cloud mass and heat fluxes from radar and synoptic data. *J. Atmos. Sci.*, **37**, 754–773.

Houze, R. A., Jr. and C. A. Leary, 1976: Comparison of convective mass and heat transports in tropical easterly waves computed by two methods. *J. Atmos. Sci.*, **33**, 424–429.

Iguchi, T., T. Kozu, R. Meneghini, J. Awaka, and K. Okamoto, 2000: Rain-profiling algorithm for the TRMM precipitation radar. *J. Appl. Meteor.*, **39**, 2038–2052.

Johnson, R. H., 1976: The role of convective-scale precipitation downdrafts in cumulus and synoptic-scale interactions. *J. Atmos. Sci.*, **33**, 1890–1910.

— 1984: Partioning tropical heat and moisture budgets into cumulus and mesoscale components: Implications for cumulus parameterization. *Mon. Wea. Rev.*, **112**, 1590–1601.

Johnson, R. H. and P. E. Ciesielski, 2000: Rainfall and radiative heating rates from TOGA COARE atmospheric budgets. *J. Atmos. Sci.*, **57**, 1497–1514.

— 2002: Characteristics of the 1998 summer monsoon onset over the northern South China Sea. *J. Meteor. Soc. Japan*, **80**, 561–578.

Johnson, R. H. and X. Lin, 1997: Episodic trade wind regimes over the western Pacific warm pool. *J. Atmos. Sci.*, **54**, 2020–2034.

Johnson, R. H. and G. S. Young, 1983: Heat and moisture budgets of tropical mesoscale anvil clouds. *J. Atmos. Sci.*, **40**, 2138–2146.

Kingsmill, D. E. and R. M. Wakimoto, 1991: Kinematic, dynamic, and thermodynamic analyses of a weakly sheared severe thunderstorm over northern Alabama. *Mon. Wea. Rev.*, **119**, 262–297.

Klemp, J. and R. Wilhelmson, 1978: The simulation of three-dimensional convective storm dynamics. *J. Atmos. Sci.*, **35**, 1070–1096.

Kozu, T. and Coauthors, 2001: Development of precipitation radar onboard the Tropical Rainfall Measuring Mission (TRMM) satellite. *IEEE Trans. Geosci. Remote Sens.*, **39**, 102–116.

Krishnamurti, T. N., S. Low-Nam, and R. Pasch, 1983: Cumulus parameterization and rainfall rates II. *Mon. Wea. Rev.*, **111**, 815–828.

Kummerow, C. and Coauthors, 2000: The status of the Tropical Rainfall Measuring Mission (TRMM) after two years in orbit. *J. Appl. Meteor.*, **39**, 1965–1982.

Lafore, J. P., J. L. Redelsperger, and G. Jaubert, 1988: Comparison between a three-dimensional simulation and doppler radar data of a tropical squall line:

Transports of mass, momentum, heat, and moisture. *J. Atmos. Sci.*, **45**, 2744–2763.

Lang, S., W.-K. Tao, J. Simpson, and B. Ferrier, 2003: Modeling of convective-stratiform precipitation processes: Sensitivity to partioning methods. *J. Appl. Meteor.*, **42**, 505–527.

Leary, C. A. and R. A. Houze Jr., 1979: Melting and evaporation of hydrometors in precipitation from the anvil clouds of deep tropical convection. *J. Atmos. Sci.*, **37**, 784–796.

— 1980: The contribution of mesoscale motions to the mass and heat fluxes of an intense tropical convective system. *J. Atmos. Sci.*, **37**, 784–796.

Lin, X. and R. H. Johnson, 1996: Heating, moistening and rainfall over the western Pacific warm pool during TOGA COARE. *J. Atmos. Sci.*, **53**, 3367–3383.

Lin, Y.-L., R. D. Farley, and H. D. Orville, 1983: Bulk parameterization of the snow field in a cloud model. *J. Clim. Appl. Meteor.*, **22**, 1065–1092.

Madden, R. A. and P. Julian, 1994: Observations of the 40-50 day oscillation tropical oscillation – a review. *Mon. Wea. Rev.*, **122**, 814–837.

Magagi, R. and A. P. Barros, 2004: Estimation of latent heating of rainfall during the onset of the Indian monsoon using TRMM PR and radiosonde data. *J. Appl. Meteor.*, **43**, 328–349.

Mapes, B. E., P. E. Ciesielski, and R. H. Johnson, 2003: Sampling errors in rawinsonde-array budgets. *J. Atmos. Sci.*, **60**, 2697–2714.

Morita, J., Y. N. Takayabu, S. Shige, and Y. Kodama, 2006: Analysis of rainfall characteristics of the Madden-Julian oscillation using TRMM satellite data. *Dyn. Atmos. Oceans*, **42**, 107–126.

Nitta, T., 1972: Energy budget of wave disturbances over the Marshall Island during the years of 1956 and 1958. *J. Meteor. Soc. Japan*, **50**, 71–84.

— 1978: A diagnostic study of interaction of cumulus updrafts and downdrafts with large-scale motions in GATE. *J. Meteor. Soc. Japan*, **56**, 232–242.

— 1980: Preliminary budget computations over the bay of Bengal during summer MONEX. *FGGE Operational Report*, **9**, 145–150.

Nitta, T. and S. Esbensen, 1974: Heat and moisture budget analyses using BOMEX data. *Mon. Wea. Rev.*, **102**, 17–28.

Okamoto, K., 2003: A short history of the TRMM precipitation radar. *Cloud Systems, Hurricanes and The Tropical Rainfall Measurement Mission (TRMM): A Tribute to Dr. Joanne Simpson*, Amer. Meteor. Soc., number 51 in Meteor. Monogr., 187–195.

Rajendran, J., T. N. Krishnamurti, V. Misra, and W.-K. Tao, 2004: An emprical cumulus parameterization scheme for a global spectral model. *J. Meteor. Soc. Japan*, **82**, 989–1006.

Reed, R. J. and E. E. Recker, 1971: Structure and properties of synoptic-scale wave disturbances in the equatorial western Pacific. *J. Atmos. Sci.*, **28**, 1117–1133.

Rutledge, S. A. and P. V. Hobbs, 1984: The mesoscale and microscale structure and organization of clouds and precipitation in midlatitude cyclones. XII: A diagnostic modeling study of precipitation development in narrow cold-frontal rainbands. *J. Atmos. Sci.*, **41**, 2949–2972.

Schumacher, C. and R. A. Houze Jr., 2003a: Stratiform rain in the tropics as seen by the TRMM precipitation radar. *J. Climate*, **16**, 1739–1756.

— 2003b: The TRMM precipitation radar's view of shallow, isolated rain. *J. Appl. Meteor.*, **42**, 1519–1524.

Schumacher, C., R. A. Houze Jr., and I. Kraucunas, 2004: The tropical dynamical response to latent heating estimates derived from the TRMM precipitation radar. *J. Atmos. Sci.*, **61**, 1341–1358.

Shie, C.-L., W.-K. Tao, J. Simpson, and C.-H. Sui, 2003: Quasi-equibrium states in the tropics simulated by a cloud-resolving model. Part I: Specific features and budget analysis. *J. Climate*, **16**, 817–833.

Shige, S., H. Sasaki, K. Okamoto, and T. Iguchi, 2006: Validation of rainfall estimates from the TRMM precipitation radar and microwave imager using a radiative transfer model: 1. Comparison of the version-5 and -6 products. *Geophys. Res. Lett.*, **33**, L13803, doi:10.1029/2006GL026350.

Shige, S. and T. Satomura, 2000: The gravity wave response in the troposphere around deep convection. *J. Meteor. Soc. Japan*, **78**, 789–801.

Shige, S., Y. N. Takayabu, W.-K. Tao, and D. E. Johnson, 2004: Spectral retrieval

of latent heating profiles from TRMM PR data. Part I: Development of a model-based algorithm. *J. Appl. Meteor.*, **43**, 1095–1113.

Shige, S., Y. N. Takayabu, W.-K. Tao, and C.-L. Shie, 2007: Spectral retrieval of latent heating profiles from TRMM PR data. Part II: Algorithm improvement and heating estimates over tropical ocean regions. *J. Appl. Meteor. Climatol.*, accepted.

Simpson, J., R. F. Adler, and G. R. North, 1988: A proposed satellite Tropical Rainfall Measuring Mission (TRMM). *Bull. Amer. Meteor. Soc.*, **69**, 278–295.

Simpson, J., C. Kummerow, W.-K. Tao, and R. F. Adler, 1996: On the Tropical Rainfall Measuring Mission (TRMM). *Meteor. and Atmos. Phys.*, **60**, 19–36.

Simpson, J. and W.-K. Tao, 1993: Goddard cumulus ensemble model. Part II: Applications for studying cloud precipitating processes and for NASA TRMM. *Terr. Atmos. Oceanic Sci.*, **4**, 73–116.

Soong, S.-T. and Y. Ogura, 1980: Response of tradewind cumuli to large-scale processes. *J. Atmos. Sci.*, **37**, 2035–2050.

Soong, S.-T. and W.-K. Tao, 1980: Response of deep tropical cumulus clouds to mesoscale processes. *J. Atmos. Sci.*, **37**, 2016–2034.

— 1984: A numerical study of the vertical transport of momentum in a tropical rainband. *J. Atmos. Sci.*, **41**, 1049–1061.

Stith, J. L., J. E. Dye, A. Bansemer, A. J. Heymsfield, C. A. Grainger, W. A. Pe-

tersen, and R. Cifelli, 2002: Microphysical observations of tropical clouds. *J. Appl. Meteor.*, **41**, 97–117.

Sui, C.-H., K.-M. Lau, W.-K. Tao, and J. Simpson, 1994: The tropical water and energy cycles in a cumulus ensemble model. Part I: Equilibrium climate. *J. Atmos. Sci.*, **51**, 711–728.

Takayabu, Y. N., 2002: Spectral representation of rain features and diurnal variations observed with TRMM PR over the equatorial area. *Geophys. Res. Lett.*, **29**, 1584, doi:10.1029/2001GL014113.

Tao, W.-K., 2003: Goddard Cumulus Ensemble (GCE) model: Application for understanding precipitation processes. *Cloud Systems, Hurricanes and The Tropical Rainfall Measurement Mission (TRMM): A Tribute to Dr. Joanne Simpson*, Amer. Meteor. Soc., number 51 in Meteor. Monogr., 107–137.

Tao, W.-K. and Coauthors, 2003: Microphysics, radiation and surface processes in the Goddard Cumulus Ensemble (GCE) model. *Meteor. Atmos. Phys.*, **82**, 97–137.

— 2006: Retrieval of latent heating from TRMM measurements. *Bull. Amer. Meteor. Soc.*, **87**, 1555–1572.

Tao, W.-K., S. Lang, J. Simpson, and R. Adler, 1993a: Retrieval algorithms for estimating the vertical profiles of latent heat release: Their applications for TRMM. *J. Meteor. Soc. Japan*, **71**, 685–700.

Tao, W.-K., S. Lang, J. Simpson, W. Olson, D. Johnson, B. Ferrier, C. Kummerow,

and R. Adler, 2000: Vertical profiles of latent heat release and their retrieval for TOGA COARE convective systems using a cloud resolving vodel, SSM/I, and ship-borne radar data. *J. Meteor. Soc. Japan*, **78**, 333–355.

Tao, W.-K., S. Lang, J. Simpson, C.-H. Sui, B. Ferrier, and M.-D. Chou, 1996: Mechanisms of cloud-radiation interaction in the tropics and midlatitudes. *J. Atmos. Sci.*, **53**, 2624–2651.

Tao, W.-K., C.-L. Shie, J. Simpson, S. Braun, R. H. Johnson, and P. E. Ciesielski, 2003: Convective systems over the South China Sea: Cloud-resolving model simulations. *J. Atmos. Sci.*, **60**, 2929–2956.

Tao, W.-K. and J. Simpson, 1993: Goddard cumulus ensemble model. Part I: Model description. *Terr. Atmos. Oceanic Sci.*, **4**, 35–72.

Tao, W.-K., J. Simpson, and S.-T. Soong, 1987: Statistical properties of a cloud ensemble: A numerical study. *J. Atmos. Sci.*, **44**, 3175–3187.

Tao, W.-K., J. Simpson, C.-H. Sui, B. Ferrier, S. Lang, J. Scala, M.-D. Chou, and K. Pickering, 1993b: Heating, moisture, and water budgets of tropical and mid-latitude squall lines: Comparisons and sensitivity to long radiation. *J. Atmos. Sci.*, **50**, 673–690.

Tao, W.-K. and S.-T. Soong, 1986: A study of the response of deep tropical clouds to mesoscale processes: Three-dimensional numerical experiments. *J. Atmos. Sci.*, **43**, 2653–2676.

Thompson, R. M. J., S. W. Payne, E. E. Recker, and R. J. Reed, 1979: Structure

and properties of synoptic-scale wave disturbances in the intertropical convergence zone of the eastern Atlantic. *J. Atmos. Sci.*, **36**, 53–72.

Webster, P. J. and R. Lukas, 1992: TOGA COARE: The coupled ocean-atmosphere response experiment. *Bull. Amer. Meteor. Soc.*, **73**, 1377–1416.

Yanai, M., S. Esbensen, and J.-H. Chu, 1973: Determination of bulk properties of tropical cloud clusters from large-scale heat and moisture budgets. *J. Atmos. Sci.*, **30**, 611–627.

Yanai, M. and R. H. Johnson, 1993: Impacts of cumulus convection on thermodynamic fields. *The Representation of Cumulus Convection in Numerical Models*, Amer. Meteor. Soc., number 46 in Meteor. Monogr., 39–62.

Yuter, S. E. and R. A. Houze Jr., 1995: Three-dimensional kinematic and microphysical evolution of florida cumulonimbus. Part II: Frequency distribution of vertical velocity, reflectivity, and differential reflectivity. *Mon. Wea. Rev.*, **123**, 1941–1963.

Yuter, S. E., R. A. Houze Jr., E. A. Smith, T. T. Wilheit, and E. Zipser, 2005: Physical characterization of tropical oceanic convection observed in KWAJEX. *J. Appl. Meteor.*, **44**, 385–415.

Figure captions

Fig.1. Diagram showing the procedure for refining and validating the spectral latent heating (SLH) algorithm. Letters denote convective and stratiform classification (C/S), precipitation top height (PTH), the precipitation rate at the lowest observable level (P_s), and the precipitation rate at the melting level (P_m). The "?" means to compare and examine the Q_2 profiles reconstructed from the SLH algorithm with the heating profiles from model simulations. This consistency check is a necessary precondition for the application of the algorithm to actual TRMM PR data.

Fig.2. Eight-day average profiles of the GCE-simulated heat budget [(a) LH, and Q_{1R} (b) without and (c) with horizontal eddy heat flux] and moisture budget [(d) NC, and Q_2 (b) without and (c) with horizontal eddy heat flux] for the total (solid), convective (dashed), stratiform (dotted) and non-precipitating (thin solid) regions for the TOGA COARE (19–26 December 1992) case.

Fig.3. Eight-day average profiles of the GCE-simulated moisture budget [(a) NC, and Q_2 (b) without and (c) with horizontal eddy heat flux] for the total (solid), convective (dashed), stratiform (dotted) and non-precipitating (thin solid) regions for the TOGA COARE (11–17 December 1992) case.

Fig.4. Ensemble-mean, GCE-simulated Q_{2p} profiles, plotted as functions of precipitation top height (PTH) from convective (a) and stratiform (b) regions, and precipitation rates at the melting level

from anvil regions (c). Contours indicate values of confidence interval for the mean at the 95 % level with Student's-t test. Contour interval is 2.0 K h^{-1} for convective and 1.0 K h^{-1} for stratiform and anvil. Thresholds of 0.3 mm h^{-1} are used for the precipitation top detection.

Fig.5. Diagram showing the procedure for deriving latent heating profiles using the spectral latent heating (SLH) algorithm. See the text for details.

Fig.6. Eight-day averaged profiles of Q_{2p} reconstructed by the SLH algorithm with the COARE lookup table (thick solid line) and Q_2 simulated by the GCE model (dotted line) for the (a) COARE (19–26 Dec 1992) case, (b) GATE (Sep 1–8 1974) case, (c) SCSMEX (Jun 2–9 1998) and (d) KWAJEX (Sep 6–13 1999), respectively. Leftmost panels are for the convective regions, center-left panels for the stratiform regions, center-right panels for the non-precipitating regions and the rightmost panels are for the total regions. Thin solid lines indicate differences between the SLH-reconstructed and the GCE-simulated profiles.

Fig.7. The rms error in the horizontal averaged profiles between the SLH algorithm-reconstructed Q_{2p} and the GCE-simulated Q_2 for the (a) COARE, (b) GATE, (c) SCSMEX, and (d) KWAJEX cases.

Fig.8. Heating from diagnostic calculations (Johnson and Ciesielski 2002) and the SLH2 algorithm using version 6 of the TRMM PR data sets for SCSMEX (15 May - 20 June 1998).

Fig.9. Monthly mean rainfall (mm day^{-1}) derived from PR2A25 Version 6 for (a) February 1998 and (b) February 1999. The drying/moistening profiles will be compared and examined for the various geographic locations identified by the boxes. [From Shige et al. (2007)]

Fig.10. Monthly (February 1998) mean total, convective and stratiform Q_{2p} profiles derived from the SLH2 algorithm for various locations. Total heating profiles derived from the CSH algorithm are also shown. The geographic areas are the (a) western Pacific, (b) central Pacific, (c) east Pacific, (d) south Pacific, (e) Indian Ocean, and (f) Atlantic Ocean. Note that the abscissa scales are the same except for Fig. 10f

Fig.11. Same as Fig. 10 except for February 1999.

Fig.12. Contoured-frequency-by-altitude diagrams (CFADs) of monthly (February 1998) total Q_{2p} profiles at 0.5^o resolution derived from the SLH2 algorithm for various locations. The geographic areas are the (a) western Pacific, (b) central Pacific, (c) east Pacific, (d) south Pacific, (e) Indian Ocean, and (f) Atlantic Ocean. The bin size is 0.5 K. CFAD contour interval: 1% for values $< 4\%$ and 4% above. Values $> 20\%$ are shaded.

Fig.13. Same as Fig. 12 except for February 1999.

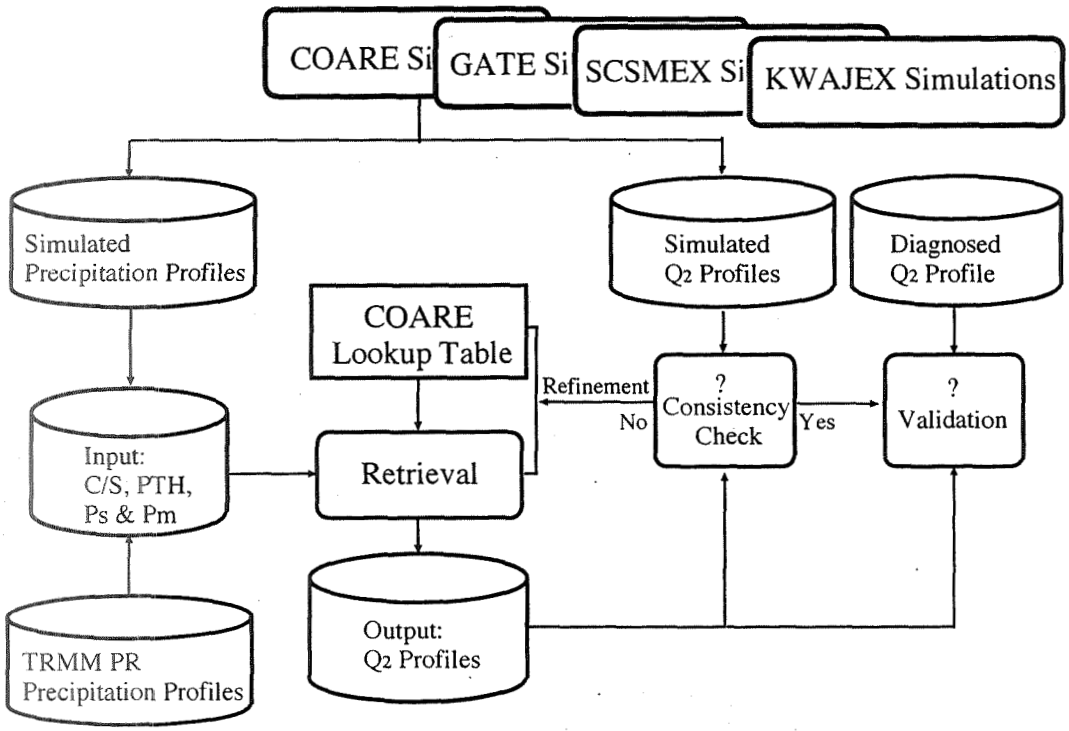

Fig. 1. Diagram showing the procedure for refining and validating the spectral latent heating (SLH) algorithm. Letters denote convective and stratiform classification (C/S), precipitation top height (PTH), the precipitation rate at the lowest observable level (P_s), and the precipitation rate at the melting level (P_m). The "?" means to compare and examine the Q_2 profiles reconstructed from the SLH algorithm with the heating profiles from model simulations. This consistency check is a necessary precondition for the application of the algorithm to actual TRMM PR data.

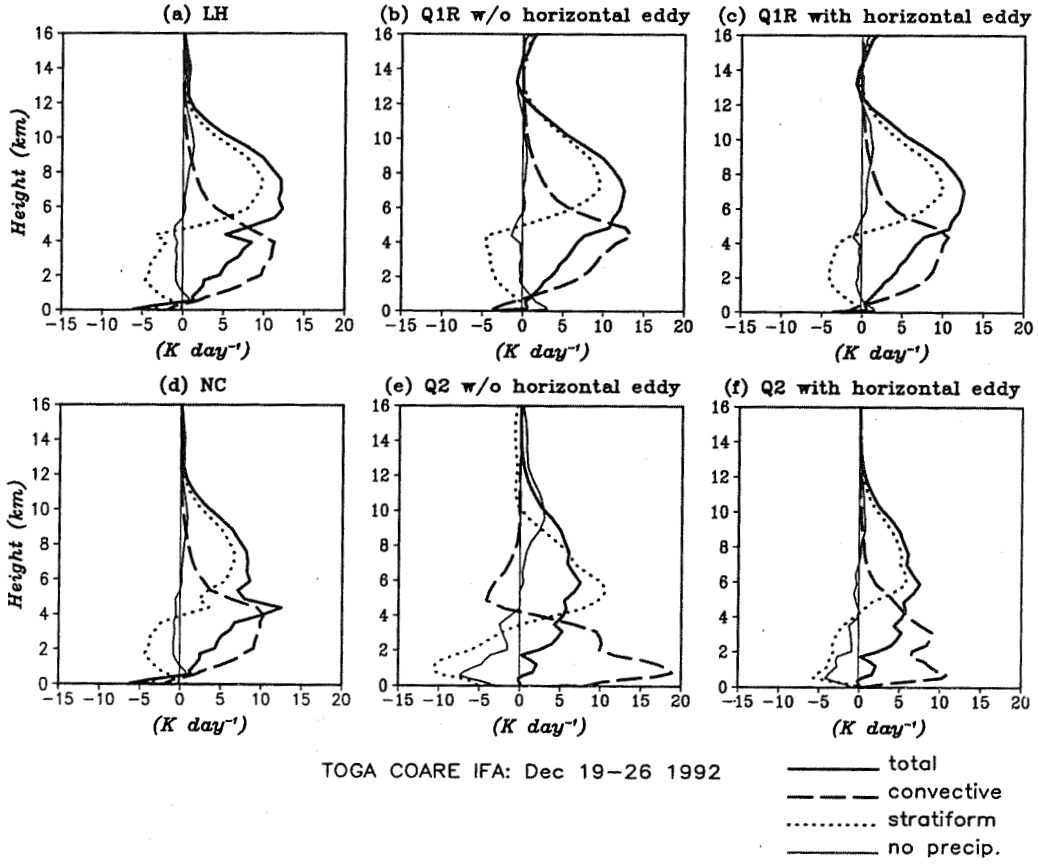

Fig. 2. Eight-day average profiles of the GCE-simulated heat budget [(a) LH, and Q_{1R} (b) without and (c) with horizontal eddy heat flux] and moisture budget [(d) NC, and Q_2 (b) without and (c) with horizontal eddy heat flux] for the total (solid), convective (dashed), stratiform (dotted) and non-precipitating (thin solid) regions for the TOGA COARE (19–26 December 1992) case.

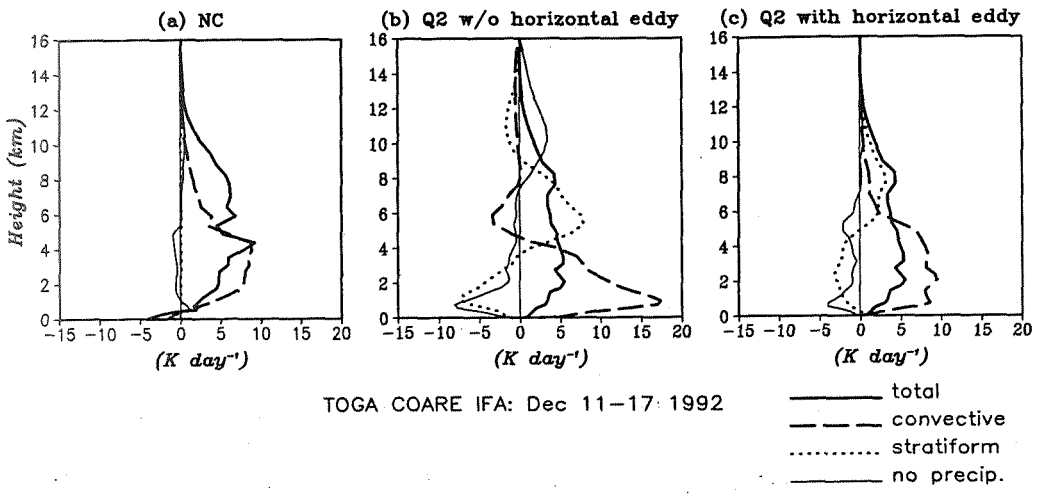

Fig. 3. Eight-day average profiles of the GCE-simulated moisture budget [(a) NC, and Q_2 (b) without and (c) with horizontal eddy heat flux] for the total (solid), convective (dashed), stratiform (dotted) and non-precipitating (thin solid) regions for the TOGA COARE (11–17 December 1992) case.

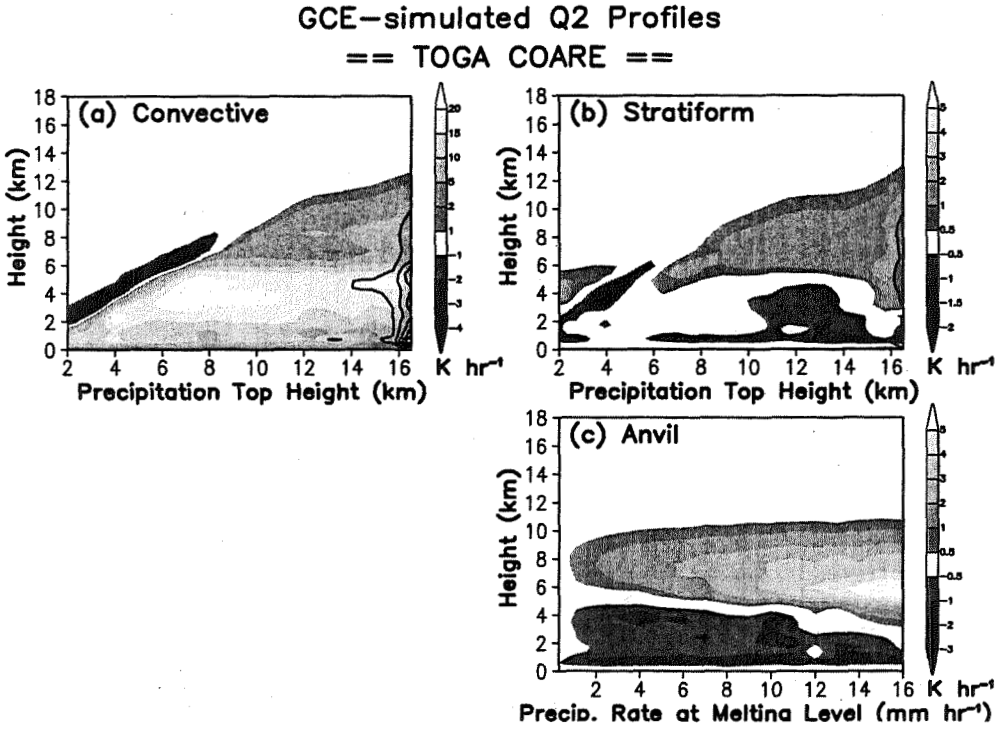

Fig. 4. Ensemble-mean, GCE-simulated Q_{2p} profiles, plotted as functions of precipitation top height (PTH) from convective (a) and stratiform (b) regions, and precipitation rates at the melting level from anvil regions (c). Contours indicate values of confidence interval for the mean at the 95 % level with Student's-t test. Contour interval is 2.0 K h^{-1} for convective and 1.0 K h^{-1} for stratiform and anvil. Thresholds of 0.3 mm h^{-1} are used for the precipitation top detection.

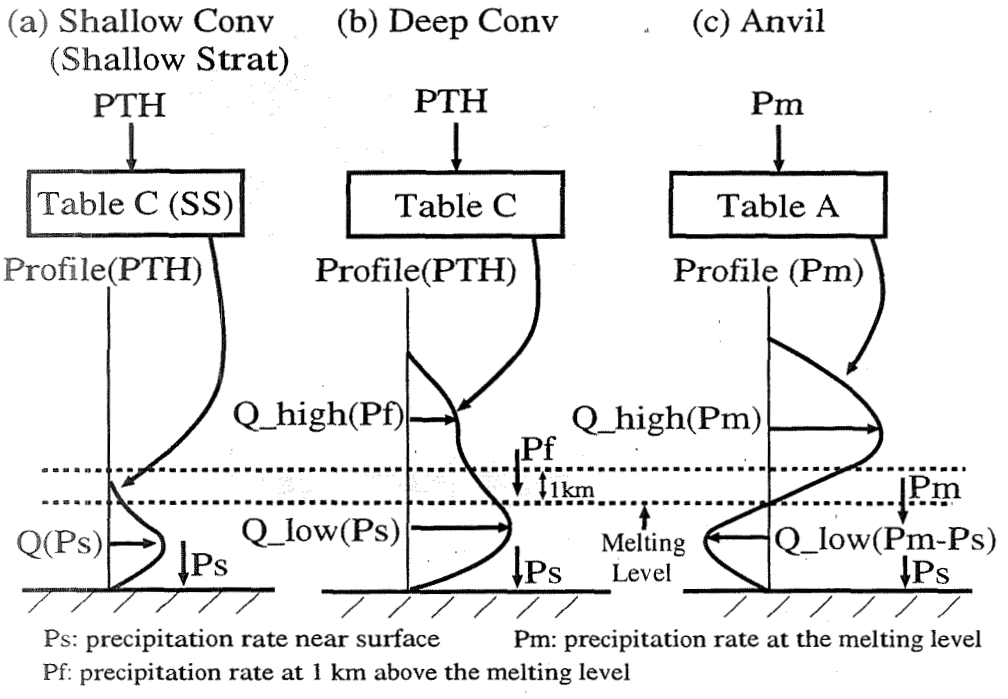

Fig. 5. Diagram showing the procedure for deriving latent heating profiles using the spectral latent heating (SLH) algorithm. See the text for details.

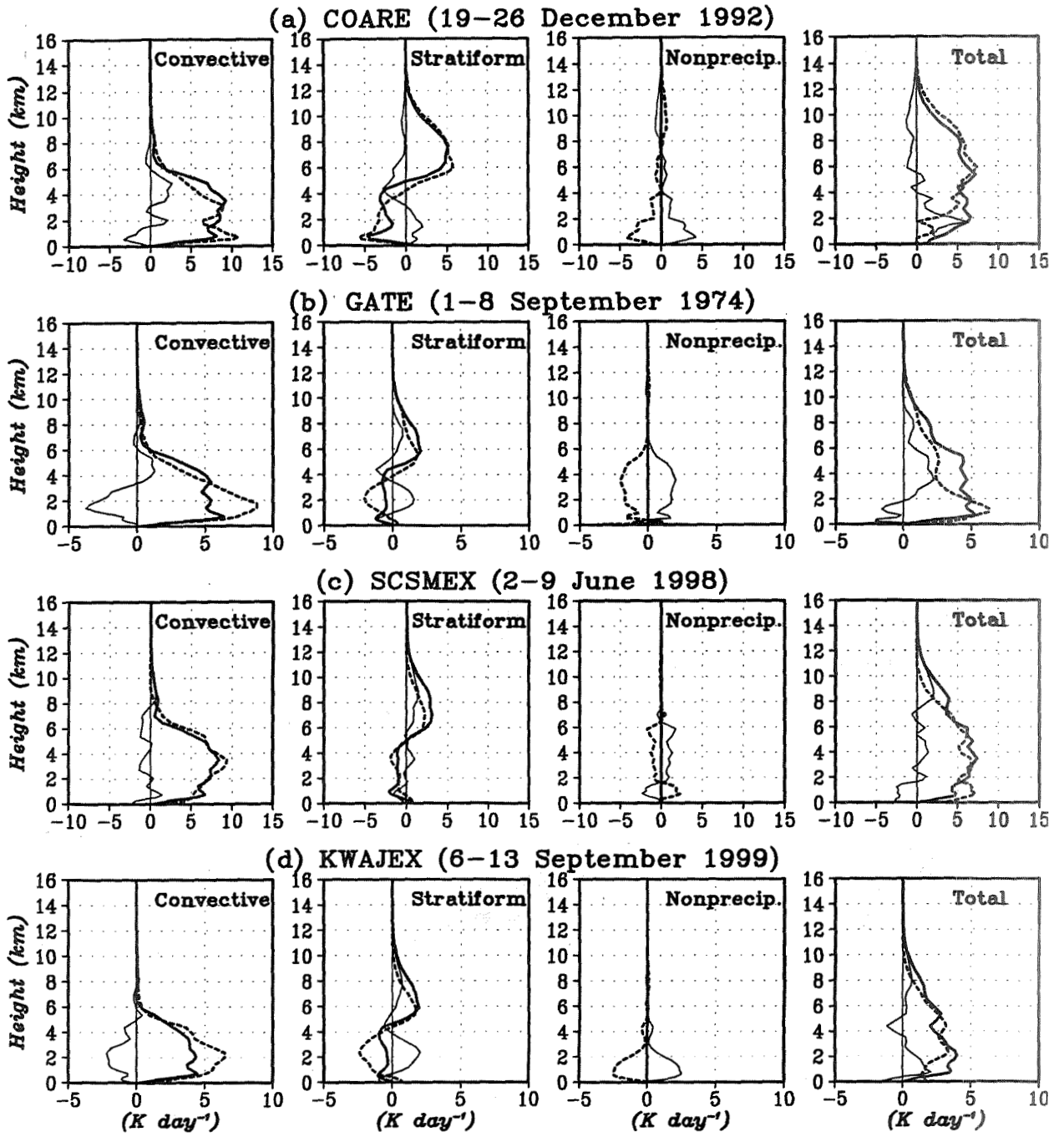

Fig. 6. Eight-day averaged profiles of Q_{2p} reconstructed by the SLH algorithm with the COARE lookup table (thick solid line) and Q_2 simulated by the GCE model (dotted line) for the (a) COARE (19–26 Dec 1992) case, (b) GATE (Sep 1–8 1974) case, (c) SCSMEX (Jun 2–9 1998) and (d) KWAJEX (Sep 6–13 1999), respectively. Leftmost panels are for the convective regions, center-left panels for the stratiform regions, center-right panels for the non-precipitating regions and the rightmost panels are for the total regions. Thin solid lines indicate differences between the SLH-reconstructed and the GCE-simulated profiles.

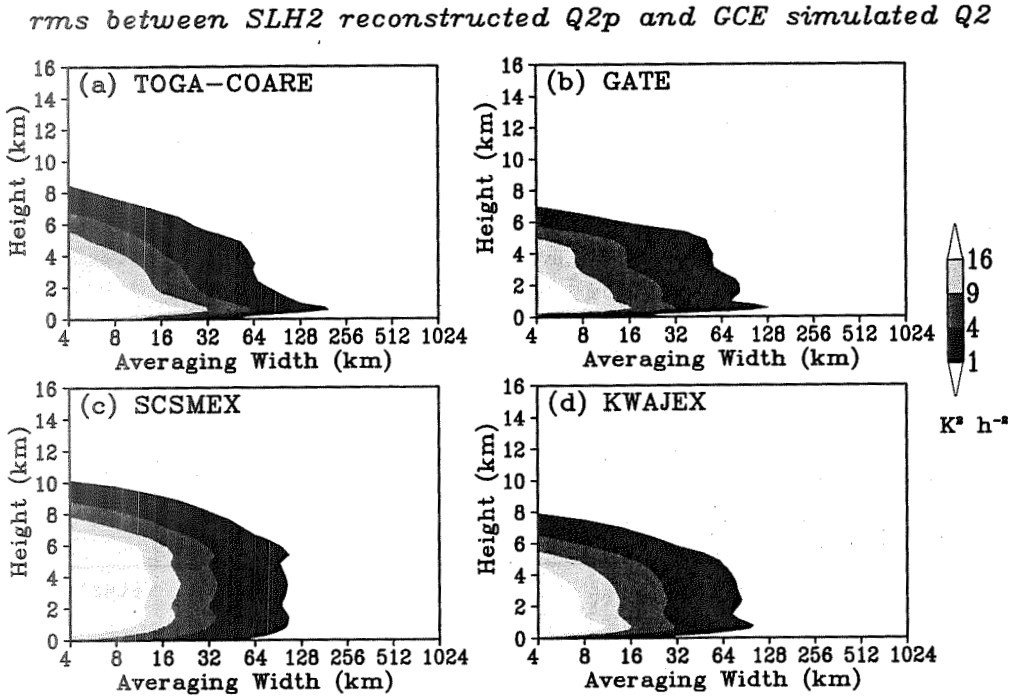

Fig. 7. The rms error in the horizontal averaged profiles between the SLH algorithm-reconstructed Q_{2p} and the GCE-simulated Q_2 for the (a) COARE, (b) GATE, (c) SCSMEX, and (d) KWAJEX cases.

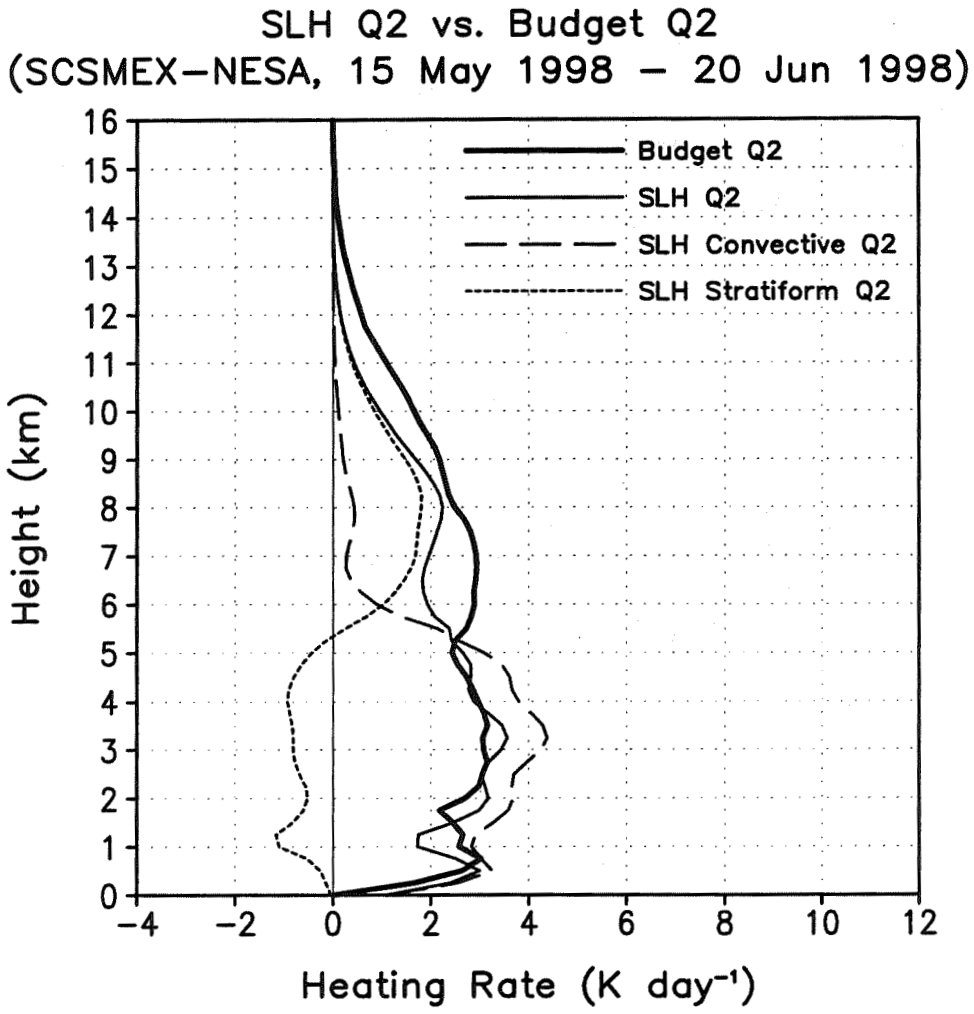

Fig. 8. Heating from diagnostic calculations (Johnson and Ciesielski 2002) and the SLH2 algorithm using version 6 of the TRMM PR data sets for SCSMEX (15 May - 20 June 1998).

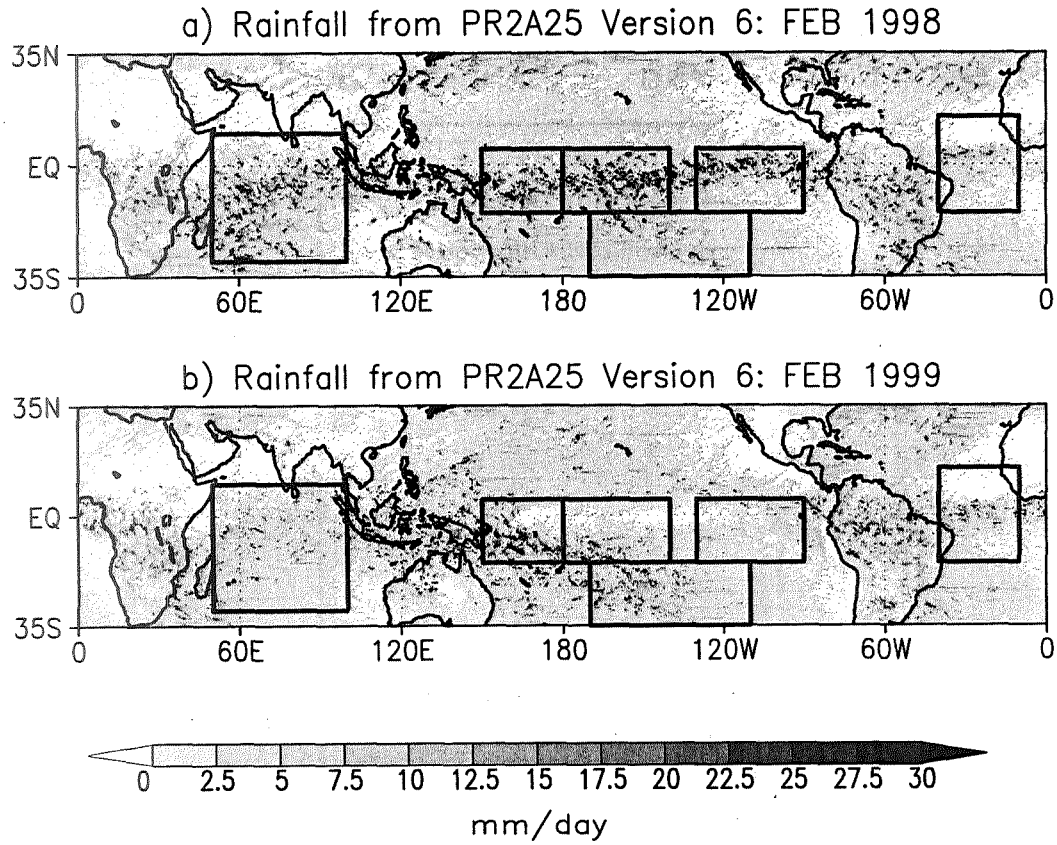

Fig. 9. Monthly mean rainfall (mm day^{-1}) derived from PR2A25 Version 6 for (a) February 1998 and (b) February 1999. The drying/moistening profiles will be compared and examined for the various geographic locations identified by the boxes. [From Shige et al. (2007)]

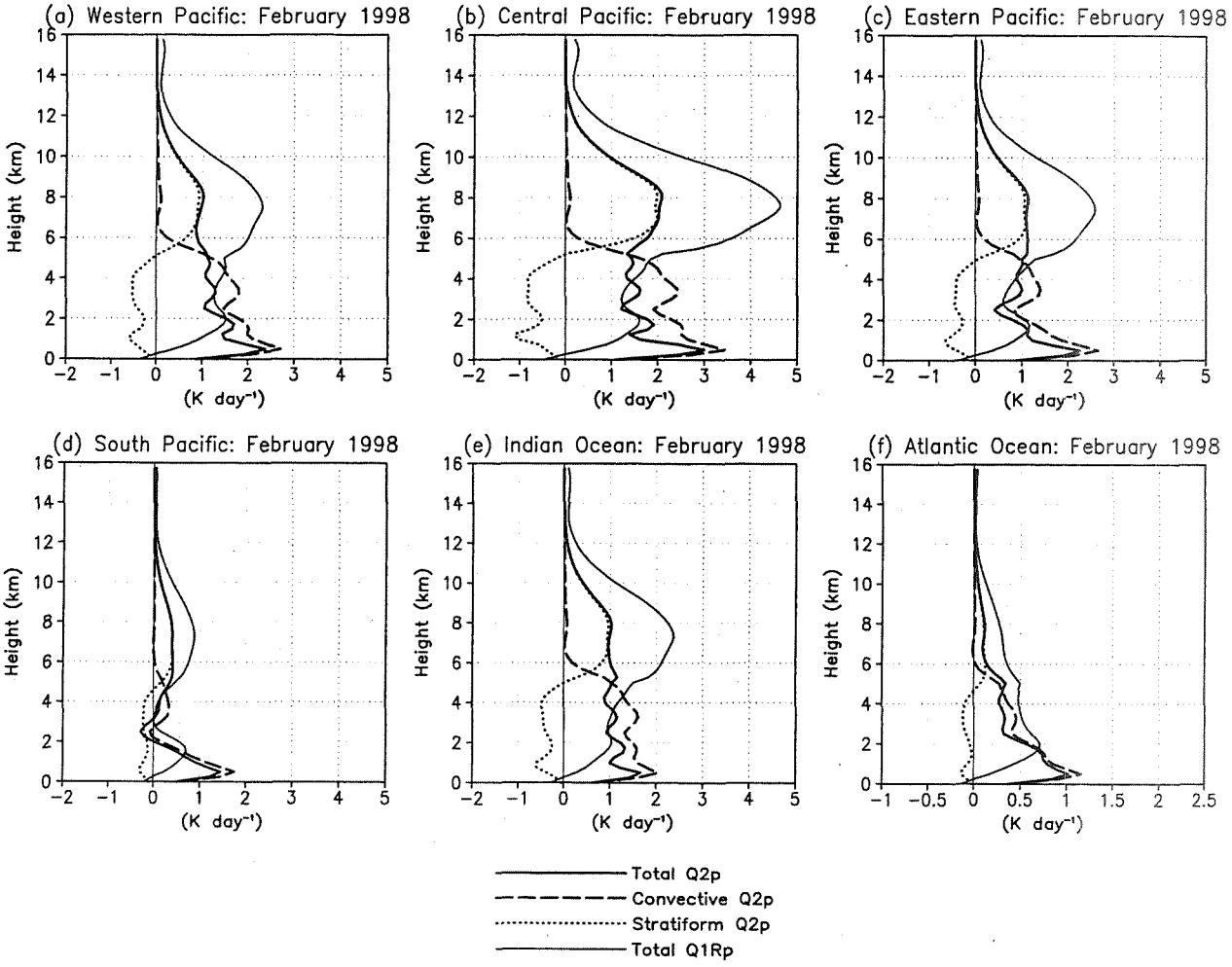

Fig. 10. Monthly (February 1998) mean total, convective and stratiform Q_{2p} profiles derived from the SLH2 algorithm for various locations. Total heating profiles derived from the CSH algorithm are also shown. The geographic areas are the (a) western Pacific, (b) central Pacific, (c) east Pacific, (d) south Pacific, (e) Indian Ocean, and (f) Atlantic Ocean. Note that the abscissa scales are the same except for Fig. 10f

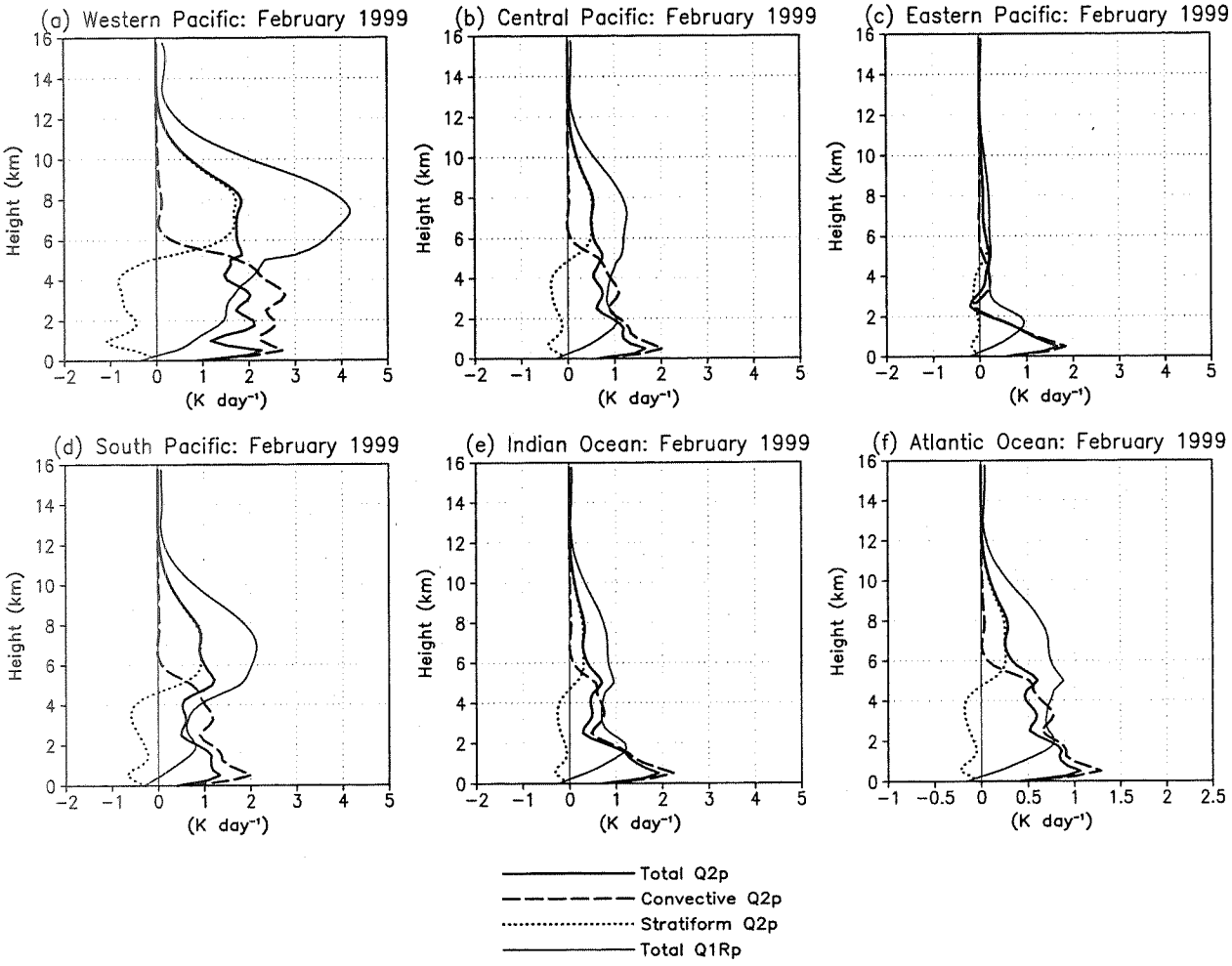

Fig. 11. Same as Fig. 10 except for February 1999.

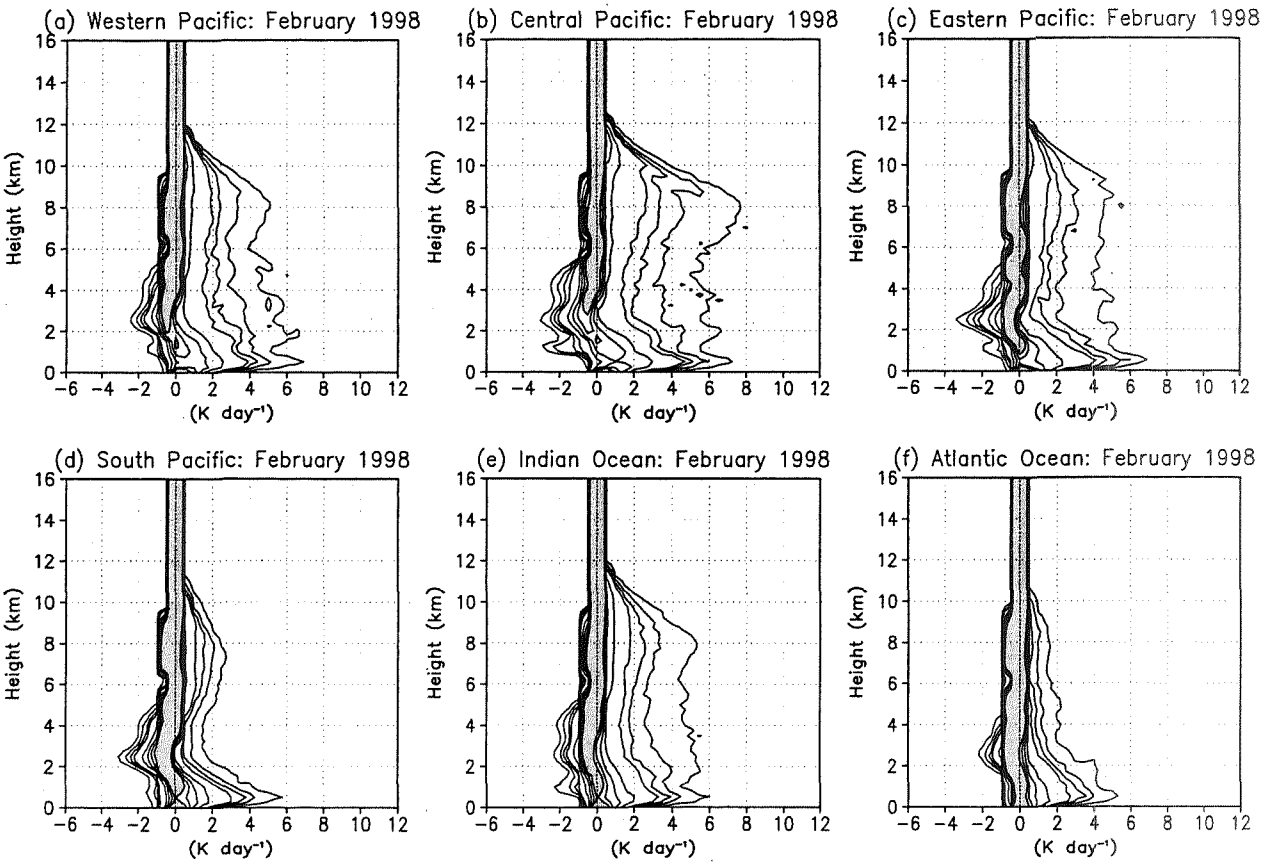

Fig. 12. Contoured-frequency-by-altitude diagrams (CFADs) of monthly (February 1998) total Q_{2p} profiles at 0.5^o resolution derived from the SLH2 algorithm for various locations. The geographic areas are the (a) western Pacific, (b) central Pacific, (c) east Pacific, (d) south Pacific, (e) Indian Ocean, and (f) Atlantic Ocean. The bin size is 0.5 K. CFAD contour interval: 1% for values $<$ 4% and 4% above. Values $>$ 20% are shaded.

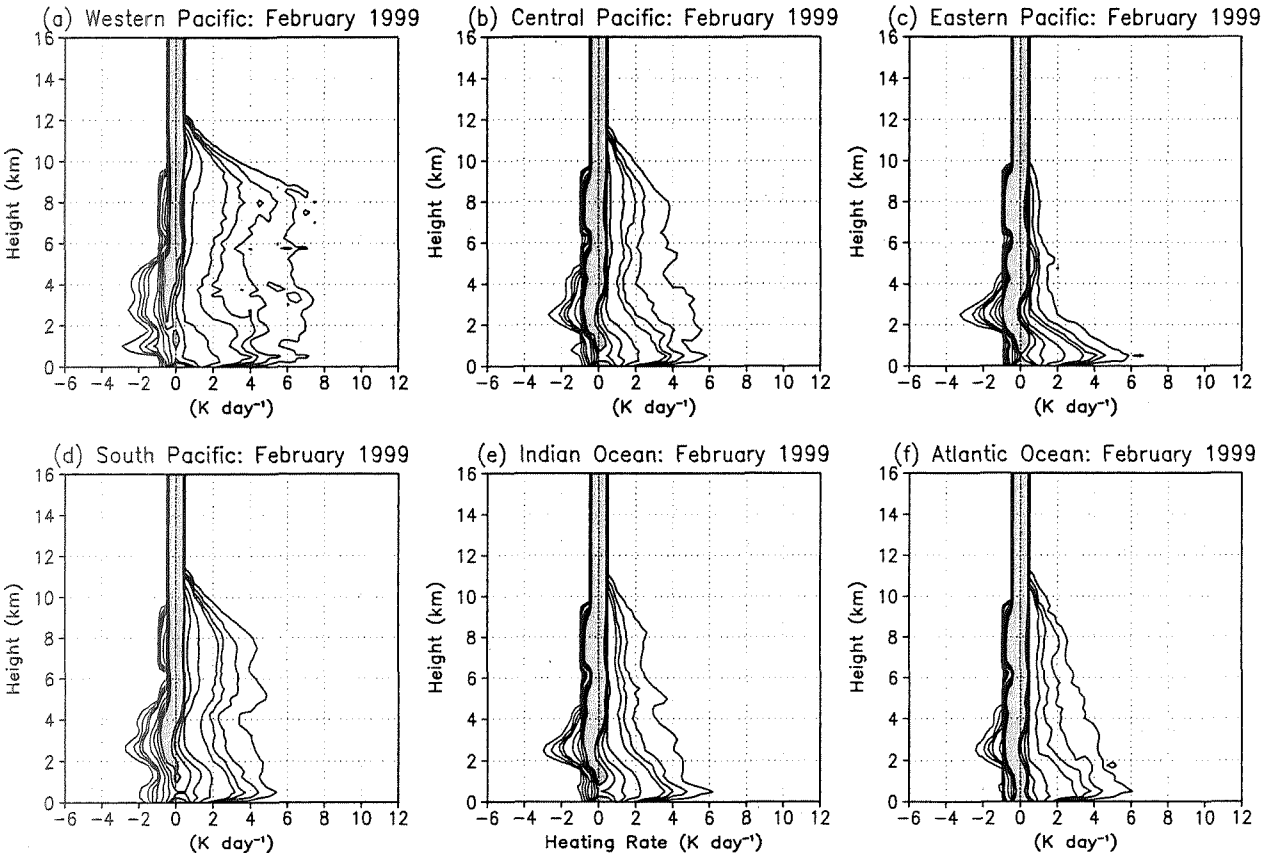

Fig. 13. Same as Fig. 12 except for February 1999.